Accepted to J. Renew. Sustain. Energy 10.1063/5.0087613

Comparison of wind turbine blade structural models of different levels of complexity against experimental data

Louis-Charles Forcier[1, a)] and Simon Joncas[1]

Department of Systems Engineering, École de technologie supérieure, 1100 Notre-Dame West Street, Montreal, Quebec, Canada, H3C 1K3

(Dated: 9 June 2022)

As the design process of a wind turbine blade is highly iterative, one needs to do the same calculations several times. During that process, the kind of structural model use must be chosen carefully trying to obtain a good compromise between precision and model setup and computation time. This paper compares four blades structural models of different levels of complexity. These models are compared to each other and with experimental results with respect to their abilities to analyze blade cross-sectional properties, natural frequencies, deflection, strains, buckling strength and composite strength. This comparison shows that even if the 3D shell finite element model is the more precise and is the only one that can manage the regions of the blade where the cross-sectional shape changes quickly, strength of material based models give accurate results. Even the simpler model, based on blade shape simplification, gives conservative and accurate results at a very low computational cost.

[a)] Electronic mail: louis-charles.forcier.1@ens.etsmtl.ca

Accepted to J. Renew. Sustain. Energy 10.1063/5.0087613

I. INTRODUCTION

Like many other components, the structural design process of a wind turbine blade is an iterative process. From one iteration to another, the structural designer has to provide blade cross-sectional properties (for instance, $\overline{EA}$, $\overline{EI}$, mass per unit length) to the aeroelastic analysis model and to perform the blade structural dimensioning and validation using the loads outputted by the aeroelastic model. Either of those can come first depending on the information available and the hypothesis used.

As a few iterations can be needed to reach the final design, the tools and models used may not be the same at each iteration. For example, the models needed for final iterations are not necessarily well suited for preliminary stages of the design process where simple and easy-to-solve models are generally preferred.

Two types of structural models are mainly used: beam models and 3D shell finite element models. Beam models are based on the strength of material theory. They are the type of model used in most of the aeroelastic codes, and they are well suited and often used for the blade cross-sectional property evaluation. However, they can also yield valuable information for the blade structural validation. Their capabilities for evaluating stresses and strains, deflection, buckling, and eigenfrequencies are not as good as those of a 3D finite element model (especially in the areas of rapid cross section change like maximum chord to root transition region), but they are sufficient for preliminary dimensioning and validation and they are much faster to set up and get results than 3D shell finite element models. It is also interesting to note that the most recent aeroelastic codes tend to include beam models that are able to manage all the material and geometric coupling between the different deformation modes of general composite beams. Therefore, complex cross-sectional analysis tools are needed in order to get all the required cross-sectional properties.

3D shell finite element models are based on surface elements with nodes having translational and rotational degrees of freedom. Commercial software offers shell finite elements with through the thickness layered material definition that are well suited for composite materials. This type of model is often used for the structural dimensioning and validation of the blade. However, with proper post-processing, a 3D shell finite element model can also be used to get the blade cross-sectional properties[1].

The blade designer then has to choose the right structural analysis model to use in a given situation. That being said, the purpose of this article is to compare wind turbine blade structural models of different levels of complexity with respect to their capability of blade design and analysis and conclude on their use at the different stages of the blade design process. These models are compared with each other and with experimental data.

The blade used as reference and the test setup are first presented. Then, four different blade structural models, from the simplest to the most complex, are described. Finally, the comparison is made about blade cross-sectional properties, natural frequencies, deflection, strains, buckling strength and composite strength.

II. WESNET BLADE AND TEST METHODOLOGY

The blades used for the experimental part of this article are those of a wind turbine designed at École de technologie supérieure and manufactured in the course of a project funded by the Natural Sciences and Engineering Research Council of Canada's Wind Energy Strategic Network (NSERC/WESNet). This 8.08 m rotor diameter turbine reaches its nominal power of 10 kW at a wind speed of 9.5 m/s. It uses the direct-drive technology and is controlled using variable speed and active pitch. The rotor auto-aligns with the wind direction due to a free yaw and downwind rotor configuration.

The 3.76 m long blades are made of epoxy-glass fiber composite and foam core. A schematic representation of the blade cross section is presented in Figure 1. The upper and lower surfaces of the airfoil and the shear web are bonded together. Both aerodynamic shells are thicker in the maximum thickness region of the airfoil (between 15 % and 45 % of chord length) to form the spar caps that support most of the blade loads. The blade external geometry is presented in Table I and the blade composite layup, in Table II. The longitudinal positions of the first column of Table II are the beginning of the ply drops. One ply is dropped each 13 mm (0.5 in). More details on blade structural design can be found in an authors' previous work[2].

For the experimental validation of the tools developed in this article, different versions of bending tests were performed. These experiments were done on a steel frame as illustrated in Figure 2. Two blades were instrumented with strain gauges on their exterior surface. On the blade surface, reflective targets were also stuck for the blade to be scanned with a 3D scanner. An EXAscan from Creaform was used. The comparison of deflected and

Accepted to J. Renew. Sustain. Energy 10.1063/5.0087613

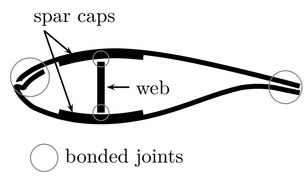

FIG. 1. Blade internal structure

TABLE I. Blade aerodynamic shape. z is the distance from the blade root, c is the airfoil chord length and θ_T is the airfoil twist angle

z [m]	θ_T [deg.]	c [m]	Airfoil
0.000	15.3	0.200	Circle
0.160	15.3	0.200	Circle
0.560	15.3	0.334	DU-97-W-300
0.760	14.5	0.318	transition
0.960	13.7	0.303	transition
1.160	12.9	0.287	transition
1.360	12.1	0.271	DU-91-W2-250
1.560	11.2	0.256	transition
1.760	10.4	0.240	transition
1.960	9.6	0.224	transition
2.160	8.8	0.208	transition
2.360	8.0	0.193	transition
2.560	7.2	0.177	DU-96-W-180
2.810	6.2	0.157	transition
3.060	5.2	0.138	transition
3.260	4.3	0.122	transition
3.460	3.2	0.106	transition
3.660	1.3	0.090	transition
3.760	0.0	0.083	DU-96-W-180

Accepted to J. Renew. Sustain. Energy 10.1063/5.0087613

TABLE II. Blade layup

Blade region, distance from blade root	Laminate
Blade root circular region	
0 mm–210 mm	[GC/CSM/$(+45/\text{-}45)_3/0_6/(+45/\text{-}45)_3$/S/ $(+45/\text{-}45)_3/0_8/(+45/\text{-}45)_3$]
Spar cap, from 15 % to 45 % of chord length	
210 mm–1074 mm	[GC/CSM/$(+45/\text{-}45)_2/0_{11}/(+45/\text{-}45)_2$]
1074 mm–2624 mm	[GC/CSM/$(+45/\text{-}45)_2/0_{10}/(+45/\text{-}45)_2$]
2624 mm–3173 mm	[GC/CSM/$(+45/\text{-}45)_2/0_6/(+45/\text{-}45)_2$]
3173 mm–3776 mm	[GC/CSM/$(+45/\text{-}45)_2/0_2/(+45/\text{-}45)_2$]
Aerodynamic shells, outside spar cap	
210 mm–960 mm	[GC/CSM/$(+45/\text{-}45)_2/0_{11}/(+45/\text{-}45)_2$]
960 mm–3776 mm	[GC/CSM/$(+45/\text{-}45)_2/0_1/(+45/\text{-}45)_2$]
Shear web	
210 mm–3776 mm	[$(+45/\text{-}45)_3$/C/$(+45/\text{-}45)_3$]

GC: gelcoat, thickness: 0.51 mm.

CSM: chopped strand mat, glass fiber with vinylester resin, thickness: 0.65 mm.

S: steel studs or 0° unidirectional glass-epoxy filler.

C: foam core, thickness : 19.05 mm.

Thickness of +45° and −45° glass-epoxy layers: 0.23 mm.

Thickness of 0° glass-epoxy layers: 0.50 mm.

undeflected scanned shapes allows the computation of the blade deflection. Note that for all flapwise bending tests, the upper surface of the airfoils is oriented towards the floor and the lower surface oriented upward.

The first test performed was a modal analysis of the blades. For that purpose, the blade root was fixed on the test support. The blade tip was manually deflected and then, quickly released. The signal of a strain gauge was recorded during the free vibration phase and a Fourier transform of this signal was used to get the eigenfrequencies of the blade.

A second test was performed in order to recreated the critical load case of the blade.

FIG. 2. Design load test setup

This was done by loading the blade at two blade stations ($z = 2.360$ m and $z = 3.500$) as shown in Figure 2. The loads were applied with manual winches and were transferred to the blade by aluminum saddles. Loads cells were also installed on the winch cables to monitor the applied loads.

A third test was intended to measure the blade cross-sectional stiffness properties. For that purpose, the blade was loaded with a mass applied near its tip. Flapwise, edgewise and torsional load cases were realized.

Finally, destructive tests were done. These tests were performed in two steps. In the first step, the blade, fixed at the root, was also simply supported in its central part ($z = 2.360$ m, the saddle closest to the root in Figure 2 was supported by a column) and loaded near its tip ($z = 3.500$ m, saddle closest to the tip in Figure 2) to create a failure in its outer part. In the second step of the destructive test, the blade was loaded at $z = 2.360$ m (saddle closest to the root in Figure 2) to generate a failure in its inner part.

III. WIND TURBINE BLADE STRUCTURAL MODELS

The four different models for blade structural analysis are now presented. From the simplest to the more complex, we have: (1) simple model, (2) classical strength of materials model, (3) cross-sectional finite element model and (4) 3D shell finite element model. For each model, the methods for the computation of eigenfrequencies, deflection, stresses, strains, buckling, strength and cross-sectional properties are presented, where applicable. The first two models are built based on literature. The third model was developed by the authors[3]. The fourth model uses commercial finite element software.

Before the description of these four models, a section is dedicated to a review of some generalities about beam cross-sectional properties.

A. Generalities about beam cross-sectional properties

For the purpose of this work, the coordinate system attached to the blade is defined as follows. The z-axis is the blade longitudinal axis. When the blade pitch angle is 0, the x-axis is in the rotor plane and point towards the direction of blade rotation, and the y-axis is normal to the rotor plane and is pointing downwind. This coordinate system is fixed to the blade and defines the flapwise and edgewise direction that correspond to the out-of-plane and in-plane directions, respectively, only when the blade pitch angle is 0.

That being said, we can define the vector of beam internal loads as

$$\mathbf{V} = \begin{bmatrix} V_x & V_y & N & M_x & M_y & M_t \end{bmatrix}^T \tag{1}$$

where V_x and V_y are the shear forces, N is the axial force, M_x and M_y are the bending moments and M_t is the torsional moment. Defining the beam reference axis displacements as χ_x, χ_y and χ_z and the beam reference axis rotations as φ_x, φ_y and φ_z, we can express the beam generalized strain vector as

$$\boldsymbol{\kappa} = \begin{bmatrix} \gamma^0_{zx} & \gamma^0_{yz} & \epsilon^0_z & \kappa_x & \kappa_y & \kappa_z \end{bmatrix}^T \tag{2}$$

where

$$\begin{aligned} \gamma^0_{zx} &= \frac{\partial \chi_x}{\partial z} - \varphi_y \\ \gamma^0_{yz} &= \frac{\partial \chi_y}{\partial z} + \varphi_x \\ \epsilon^0_z &= \frac{\partial \chi_z}{\partial z} \\ \kappa_x &= \frac{\partial \varphi_x}{\partial z} \\ \kappa_y &= \frac{\partial \varphi_y}{\partial z} \\ \kappa_z &= \frac{\partial \varphi_z}{\partial z} \end{aligned} \tag{3}$$

This describes the behavior of a Timoshenko beam.

The relation between beam internal loads $\mathbf{V}$ and beam generalized strains $\boldsymbol{\kappa}$, for a given cross section is

$$\mathbf{V} = \mathbf{K}_s \boldsymbol{\kappa} \tag{4}$$

or

$$\boldsymbol{\kappa} = \mathbf{F}_s \mathbf{V} \tag{5}$$

where $\mathbf{K}_s$ is the cross-sectional stiffness matrix, which is symmetric and $\mathbf{F}_s = \mathbf{K}_s^{-1}$ is the cross-sectional compliance matrix.

For an Euler beam, $\gamma^0_{zx} = \gamma^0_{yz} = 0$ in Eq. 3. The cross-sectional stiffness matrix then reduces to a 4×4 matrix, the terms associated with transverse shear due to shear forces being eliminated. The compliance matrix of an Euler beam model is equal to the compliance matrix of a Timoshenko beam model from which the first two rows and columns are removed.

In the particular case where the origin of the cross-sectional coordinate system is coincident with the elastic and shear centers, and the x and y-axes are the principal axes of bending, Eq. 5 reduces to

$$\begin{bmatrix} V_x \\ V_y \\ N \\ M_x \\ M_y \\ M_t \end{bmatrix} = \begin{bmatrix} k_x\overline{GA}_x & 0 & 0 & 0 & 0 & 0 \\ 0 & k_y\overline{GA}_y & 0 & 0 & 0 & 0 \\ 0 & 0 & \overline{EA} & 0 & 0 & 0 \\ 0 & 0 & 0 & \overline{EI}_x & 0 & 0 \\ 0 & 0 & 0 & 0 & \overline{EI}_y & 0 \\ 0 & 0 & 0 & 0 & 0 & \overline{GJ} \end{bmatrix} \begin{bmatrix} \gamma^0_{zx} \\ \gamma^0_{yz} \\ \epsilon^0_z \\ \kappa_x \\ \kappa_y \\ \kappa_z \end{bmatrix} \tag{6}$$

where

$$\begin{aligned} \overline{GA}_x &= \int G_{zx}\, \mathrm{d}A \\ \overline{GA}_y &= \int G_{yz}\, \mathrm{d}A \\ \overline{EA} &= \int E_z\, \mathrm{d}A \\ \overline{EI}_x &= \int E_z y^2\, \mathrm{d}A \\ \overline{EI}_y &= \int E_z x^2\, \mathrm{d}A \end{aligned} \tag{7}$$

k_x and k_y are the correction factors for transverse shear[4] and $\overline{GJ}$ is obtained from the solution of the torsion problem. Note that for an axisymmetric cross section:

$$\overline{GJ} = \int (x^2 G_{yz} + y^2 G_{zx})\, \mathrm{d}A \tag{8}$$

G_{zx} and G_{yz} are the material's shear moduli and E_x, E_y and E_z are the material's elastic moduli. The integrations are performed over the beam cross section A.

We can show that the relationship between the beam generalized strains expressed in two parallel coordinate systems (Figure 3) is

$$\boldsymbol{\kappa} = \mathbf{T}_s \boldsymbol{\kappa}' \tag{9}$$

where

$$\mathbf{T}_s = \begin{bmatrix} 1 & 0 & 0 & 0 & 0 & b \\ 0 & 1 & 0 & 0 & 0 & -a \\ 0 & 0 & 1 & -b & a & 0 \\ 0 & 0 & 0 & 1 & 0 & 0 \\ 0 & 0 & 0 & 0 & 1 & 0 \\ 0 & 0 & 0 & 0 & 0 & 1 \end{bmatrix} \tag{10}$$

The relationship between two sets of internal loads expressed in these coordinate systems is

$$\mathbf{V} = \mathbf{T}_s^{-T} \mathbf{V}' \tag{11}$$

where $\mathbf{T}_s^{-T} = (\mathbf{T}_s^{-1})^T = (\mathbf{T}_s^T)^{-1}$. The compliance matrix in the prime coordinate system is thus

$$\mathbf{F}'_s = \mathbf{T}_s^{-1} \mathbf{F}_s \mathbf{T}_s^{-T} \tag{12}$$

so that

$$\boldsymbol{\kappa}' = \mathbf{F}'_s \mathbf{V}' \tag{13}$$

The cross-sectional stiffness matrix in the prime coordinate system is accordingly

$$\mathbf{K}'_s = \mathbf{T}_s^T \mathbf{K}_s \mathbf{T}_s \tag{14}$$

so that

$$\mathbf{V}' = \mathbf{K}'_s \boldsymbol{\kappa}' \tag{15}$$

Two sets of generalized strains and internal forces, after rotation of the coordinate system (see Fig. 3), are related a follows:

$$\boldsymbol{\kappa} = \mathbf{T}_\theta \boldsymbol{\kappa}'' \tag{16}$$

and

$$\mathbf{V} = \mathbf{T}_\theta \mathbf{V}'' \tag{17}$$

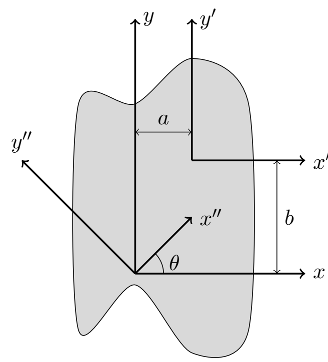

FIG. 3. Coordinate systems used to transform the cross-sectional stiffness and compliance matrices

where

$$\mathbf{T}_\theta = \begin{bmatrix} c & -s & 0 & 0 & 0 & 0 \\ s & c & 0 & 0 & 0 & 0 \\ 0 & 0 & 1 & 0 & 0 & 0 \\ 0 & 0 & 0 & c & -s & 0 \\ 0 & 0 & 0 & s & c & 0 \\ 0 & 0 & 0 & 0 & 0 & 1 \end{bmatrix} \tag{18}$$

and where $s = \sin\theta$ and $c = \cos\theta$.

The cross-sectional compliance matrix in the double prime coordinate system is then:

$$\mathbf{F}_s'' = \mathbf{T}_\theta^{-1}\mathbf{F}_s\mathbf{T}_\theta \tag{19}$$

so that

$$\boldsymbol{\kappa}'' = \mathbf{F}_s''\mathbf{V}'' \tag{20}$$

and the cross-sectional stiffness matrix in the double prime coordinate system is

$$\mathbf{K}_s'' = \mathbf{T}_\theta^{-1}\mathbf{K}_s\mathbf{T}_\theta \tag{21}$$

so that

$$\mathbf{V}'' = \mathbf{K}_s''\boldsymbol{\kappa}'' \tag{22}$$

The shear center of the cross section is defined as the point where an applied shear force does not cause torsion. So in order for a and b to be the coordinates of this point, the shear-twist coupling terms of the compliance matrix (F'_{s16} and F'_{s26} of Eq. 12) must be null. The shear center coordinates are then:

$$
\begin{aligned}
x_c &= -\frac{F_{s26}}{F_{s66}} \\
y_c &= \frac{F_{s16}}{F_{s66}}
\end{aligned}
\tag{23}
$$

The elastic center of the cross section is defined as the point where an applied axial force does not cause bending. In order for a and b to be the coordinates of this point, the extension-bending coupling terms (F'_{s34} and F'_{s35} of Eq. 12) of the cross-sectional compliance matrix must be zero. The elastic center coordinates are then:

$$
\begin{aligned}
x_e &= \frac{F_{s44}F_{s35} - F_{s45}F_{s34}}{F_{s44}F_{s55} - F_{s45}^2} \\
y_e &= \frac{F_{s45}F_{s35} - F_{s55}F_{s34}}{F_{s44}F_{s55} - F_{s45}^2}
\end{aligned}
\tag{24}
$$

When the origin of the coordinate system is also the elastic center, this coordinate system can be rotated by an angle $\theta = \theta_1$ to get the principal axes of bending which are characterized by the absence of coupling between both directions, i.e., $F''_{s45} = 0$ in Eq. 19. The orientation of the principal axes of bending is then:

$$
\theta_1 = \frac{1}{2}\arctan\left(\frac{-2F_{s45}}{F_{s55} - F_{s44}}\right) \tag{25}
$$

B. Model 1: Simple model

Several simple models for blade preliminary analysis have been proposed[5–7] (for instance). The one proposed here is based on Hansen's book[8], where the cross section is represented as shown in Figure 4. The only parts modelled are the spar caps idealized as two rectangular strips. c is the chord length and t is the airfoil thickness.

The cross-sectional inertia (about an axis parallel to the chord line and passing through the mid distance between both spar caps) is

$$
I = \frac{bt^3}{12} - \frac{b(t-2h)^3}{12} \tag{26}
$$

and the maximum strain (and absolute value of minimum strain) is

$$
\epsilon = \frac{Mt}{2EI} \tag{27}
$$

Accepted to J. Renew. Sustain. Energy 10.1063/5.0087613

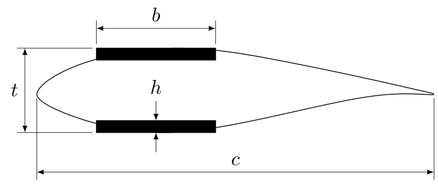

FIG. 4. Model 1: Simplified blade model

where M is the bending moment. The term "local flapwise" is used to describe this bending direction. As a simple and conservative assumption, the resultant of the in-plane and out-of-plane bending moments is supposed to be applied about an axis parallel to the chord line. E is the spar cap elastic modulus.

Using Eq. 26 and 27, the required spar cap thickness as a function of airfoil shape, material properties and bending moment is

$$h = \frac{t}{2} - \frac{1}{2}\sqrt[3]{t^3 - \frac{6Mt}{Eeb}} \tag{28}$$

where e is the failure strain.

This model can then be used for the dimensioning of the blade spar caps with Eq. 28. Once the spar cap thickness is known, at several cross sections along the blade length, a blade mass can be estimated using typical relations between spar cap mass and whole blade mass. The model can also be used for the stress and strain analysis with equations 27 and 26.

As just demonstrated, this model is well suited for preliminary structural dimensioning of wind turbine blades based on strength. However, it is not usable to evaluate natural frequencies, deflection and buckling. Also, the only cross-sectional stiffness property it computes is the local flapwise bending stiffness.

C. Model 2: Classical strength of materials model

This model is based on classical strength of materials theory. Figure 5 shows the different coordinate systems used for this analysis. Taking into account the thin-walled nature of the wind turbine blade, the integral over the area A of the cross section is computed as a line

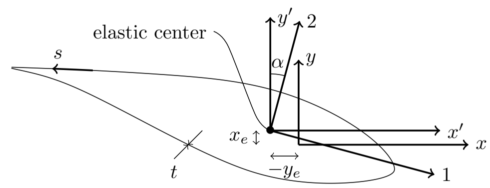

FIG. 5. Model 2: Coordinate systems for the classical strength of materials model

integral over the walls:

$$\int_A f \,\mathrm{d}A = \int_s f t \,\mathrm{d}s \tag{29}$$

where t is the wall thickness, s is the variable along the walls and f is the quantity to integrate.

This integral is then evaluated numerically by discretizing the contour in several segments and summing over these segments:

$$\int_s f t \,\mathrm{d}s \approx \sum_i f_i t_i \Delta s_i \tag{30}$$

Before performing these calculations, the contour points are translated towards the interior of the cross section by a distance of half of the wall thickness. The coordinates of the contour point then represent the mid thickness surface of the walls.

For the analysis of the extension and bending behaviour of the blade, a first set of cross-sectional properties relative to the reference coordinate system (xy) can be computed as[8]:

$$\begin{aligned}
\overline{EA} &= \int_A E \,\mathrm{d}A \\
\overline{ES}_x &= \int_A yE \,\mathrm{d}A \\
\overline{ES}_y &= \int_A xE \,\mathrm{d}A \\
\overline{EI}_x &= \int_A y^2 E \,\mathrm{d}A \\
\overline{EI}_y &= \int_A x^2 E \,\mathrm{d}A \\
\overline{EI}_{xy} &= \int_A xyE \,\mathrm{d}A
\end{aligned} \tag{31}$$

where E is the material's elastic modulus in the z-direction. For laminates, the effective elastic modulus is used. From these properties, the coordinates of the elastic center are:

$$\begin{aligned} x_e &= \frac{\overline{ES}_y}{\overline{EA}} \\ y_e &= \frac{\overline{ES}_x}{\overline{EA}} \end{aligned} \tag{32}$$

Knowing the location of the elastic center, the bending stiffness relative to this point are:

$$\begin{aligned} \overline{EI}_{x'} &= \int_A (y')^2 E\,\mathrm{d}A = \overline{EI}_x - y_e^2\overline{EA} \\ \overline{EI}_{y'} &= \int_A (x')^2 E\,\mathrm{d}A = \overline{EI}_y - x_e^2\overline{EA} \\ \overline{EI}_{x'y'} &= \int_A x'y' E\,\mathrm{d}A = \overline{EI}_{xy} - x_e y_e\overline{EA} \end{aligned} \tag{33}$$

Finally, the angle between the x'-axis and the closest principal axes of bending is:

$$\alpha = \frac{1}{2}\arctan\left(\frac{2\overline{EI}_{x'y'}}{\overline{EI}_{x'} - \overline{EI}_{y'}}\right) \tag{34}$$

and the bending stiffnesses around these axes (referred as local axes) are

$$\begin{aligned} \overline{EI}_1 &= \frac{\overline{EI}_x + \overline{EI}_y}{2} + \frac{\overline{EI}_x - \overline{EI}_y}{2}\cos 2\alpha + \overline{EI}_{xy}\sin 2\alpha \\ \overline{EI}_2 &= \frac{\overline{EI}_x + \overline{EI}_y}{2} - \frac{\overline{EI}_x - \overline{EI}_y}{2}\cos 2\alpha - \overline{EI}_{xy}\sin 2\alpha \end{aligned} \tag{35}$$

$\overline{EI}_1$ is the local flapwise bending stiffness and $\overline{EI}_2$ is the local edgewise bending stiffness. Generally, for a wind turbine blade, $\overline{EI}_2 > \overline{EI}_1$.

For a given cross section, if the local flapwise bending moment M_1, the local edgewise bending moment M_2 and the axial force N are known, it is possible to compute the axial strain of a point using:

$$\epsilon_z = \frac{M_1 y_p}{\overline{EI}_1} - \frac{M_2 x_p}{\overline{EI}_2} + \frac{N}{\overline{EA}} \tag{36}$$

where x_p and y_p are the coordinates along the 1- and 2-axes respectively and M_1 and M_2 are computed as:

$$\begin{aligned} M_1 &= M_x\cos\alpha - M_y\sin\alpha \\ M_2 &= M_x\sin\alpha + M_y\cos\alpha \end{aligned} \tag{37}$$

For the analysis of torsion, from strength of materials textbooks[9,10], the unit torsion angle of one of the cells of a multicell thin-walled beam is:

$$\kappa_z = \frac{1}{2A_i}\left(q_i\oint_i \frac{\mathrm{d}s}{Gt} - q_{i-1}\int_{i-1,i}\frac{\mathrm{d}s}{Gt} - q_{i+1}\int_{i,i+1}\frac{\mathrm{d}s}{Gt}\right) \tag{38}$$

t and G are respectively the wall thickness and shear modulus. For laminates, the effective shear modulus is used. A_i is the surface enclosed by the ith cell and q_i, q_{i-1} and q_{i+1} are respectively the shear flow in the walls of the ith cell, the shear flow in the web left to the ith cell and the shear flow in the web right to the ith cell (see Figure 6). Integrals over (i), $(i-1,i)$ and $(i,i+1)$ are respectively integral over the ith cell, the web to the left to the ith cell and the web to the right to the ith cell. Using the following notation,

$$\begin{aligned}\delta_i &= \oint_i \frac{\mathrm{d}s}{Gt}\\ \delta_{i,j} &= \int_{i,j} \frac{\mathrm{d}s}{Gt}\end{aligned} \tag{39}$$

Eq. 38 can be written as

$$2A_i\kappa_z = q_i\delta_i - q_{i-1}\delta_{i-1,i} - q_{i+1}\delta_{i,i+1} \tag{40}$$

Knowing that each cell must have the same unit torsion angle κ_z, the previous equation is repeated for each of the n cells of the beam. This results in a system of n equations to compute the shear flow q_i in each cell:

$$2\kappa_z\mathbf{A} = \boldsymbol{\delta}\mathbf{q} \tag{41}$$

where

$$\begin{aligned}\mathbf{A} &= \begin{bmatrix} A_1 & A_2 & A_3 & \dots & A_n \end{bmatrix}^T\\ \mathbf{q} &= \begin{bmatrix} q_1 & q_2 & q_3 & \dots & q_n \end{bmatrix}^T\\ \boldsymbol{\delta} &= \begin{bmatrix} \delta_1 & -\delta_{1,2} & 0 & 0 & \cdots & 0 & 0\\ -\delta_{1,2} & \delta_2 & -\delta_{2,3} & 0 & \cdots & 0 & 0\\ 0 & -\delta_{2,3} & \delta_3 & -\delta_{3,4} & \cdots & 0 & 0\\ \vdots & \vdots & \vdots & \vdots & \ddots & 0 & 0\\ 0 & 0 & 0 & 0 & 0 & -\delta_{n-1,n} & \delta_n \end{bmatrix}\end{aligned} \tag{42}$$

From equilibrium,

$$M_t = 2\mathbf{A}^T\mathbf{q} \tag{43}$$

where M_t is the torsion moment. Introducing the torsional stiffness $\overline{GJ}$:

$$M_t = \overline{GJ}\kappa_z \tag{44}$$

Accepted to J. Renew. Sustain. Energy 10.1063/5.0087613

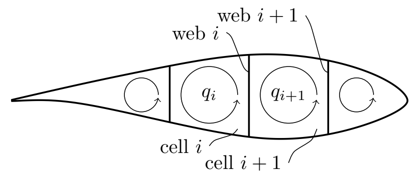

FIG. 6. Model 2: Torsion analysis of a multicell thin-walled beam

From Eq. 41, 43 and 44, the torsional rigidity can be computed as:

$$\overline{GJ} = 4\mathbf{A}^T \boldsymbol{\delta}^{-1}\mathbf{A} \tag{45}$$

The deflection analysis procedure is as follows[8]. Assuming that the applied forces (p_x, p_y and p_z) and moments (m_x, m_y and m_z) per unit length are known at n different points from the blade root to the blade tip and assuming a linear variation between these points, the internal load distribution at each of these points (V_x, V_y, N, M_x, M_y and M_t) can be computed numerically.

For each point, the beam curvature can be computed by first transferring the bending moments in the principal axis of bending and then, by evaluating the curvatures around these axes. Finally, these curvatures are converted into the xy-coordinate system.

The axial and torsional beam generalized deformations can be evaluated with:

$$\begin{aligned} \epsilon_x^{0,i} &= \frac{N^i}{\overline{EA}^i} \\ \kappa_z^i &= \frac{M_t^i}{\overline{GJ}^i} \end{aligned} \tag{46}$$

Assuming a linear variation of these beam deformations between loading points, the beam rotations and deflections can be computed numerically by solving Eq. 3 assuming that $\gamma_{zx}^0 = \gamma_{yz}^0 = 0$. By doing so, the effect of transverse shear is neglected, following the Euler-Bernoulli hypothesis.

For the modal analysis, the blade mass distribution is required. Following the same procedure as for the calculation of the cross-sectional stiffness properties, the mass per unit length m' can be computed at some location along the blade length as:

$$m' = \int_A \rho \, \mathrm{d}A \tag{47}$$

Accepted to J. Renew. Sustain. Energy 10.1063/5.0087613

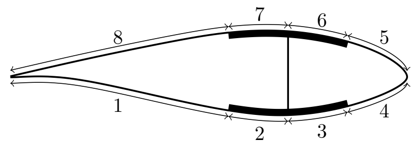

FIG. 7. Model 2: Example of panels for buckling analysis

where ρ is the material density. The modal analysis procedure used here[8] allows the computation of the first flapwise and edgewise bending modes, the most important for blade design.

For the buckling analysis, at a given cross section, the blade exterior surface is separated in different panels. A separation between two adjacent panels occurs each time (1) a web is connected to the blade surface and (2) there is a change in the laminate. For instance, in Figure 7, the cross section is separated in 8 panels. For each panel, the width b is computed as the sum of the length of the elements forming the panel and the critical compressive force per unit length is calculated using the conservative infinite length (in the blade longitudinal direction) buckling solution for flat panel simply supported on all sides[11] :

$$N_{cr} = \frac{2\pi^2}{b^2}\left(\sqrt{D_{11}D_{22}} + D_{12} + 2D_{66}\right) \tag{48}$$

where D_{11}, D_{22}, D_{12} and D_{66} are the panel bending stiffnesses obtained from the classical lamination theory[11–14].

For each panel, the mean (along its width) compressive force per unit length N_z is also computed. For each element, N_z is computed as:

$$N_z = \sigma_z t = E_z \epsilon_z t \tag{49}$$

where t is the panel thickness and E_z is its modulus of elasticity (effective modulus for laminates).

A buckling failure index can then be computed as:

$$F_{\text{buckling}} = \frac{N_z}{N_{cr}} \tag{50}$$

D. Model 3: Cross-sectional finite element model

The third model for blade structural analysis is based on a finite element discretization of the cross section. This framework, sometimes called Nonhomogeneous Anisotropic Beam

FIG. 8. Model 3: Example of blade cross-sectional mesh for analysis

Section Analysis (NABSA) was proposed by Giavotto et al.[15] and used by Blasques et al.[16–19]. It uses triangular and quadrilateral elements to discretize the beam cross section. Capitalizing on the fact that wind turbine blades are thin-walled structures, the authors have added line finite elements to this framework, allowing modelling thin-walled cross sections[3]. Figure 8 shows an example of blade cross-sectional mesh for this method.

This method allows the computation of a 6×6 cross-sectional stiffness matrix at different points along the blade length. The post-processing of the results also allows the computation of the stresses and strains in the cross sections.

When it is needed to model the whole blade behavior (for deflection and modal analysis), the blade is discretized using 3-node Timoshenko beam finite elements.

E. Model 4: 3D shell finite element model

The use of 3D finite element models for structural analysis of wind turbine blades is common. Most of the time, due to the thin-walled topology of these structures, shell finite elements are employed. As the exterior shape of the blade is the reference shape for aerodynamics, the finite element mesh is frequently located on this surface and the element thickness is built towards the blade interior.

The particularity of this model over the three previous is that it is able to manage the effects of the variation of the cross-sectional shape of the beam along its length. However, it takes more work to set up the model.

The use of this kind of model is well documented for the computation of natural frequencies, deflection, stresses, strains and buckling[20–24] (for instance). However, a difficulty arises for computing the blade cross-sectional properties needed for the aeroelastic analysis and it is to this task that the remaining of this section is dedicated.

To compute the cross-sectional properties from a 3D finite element model, we need to know, at different locations along blade length, the internal loads and the beam generalized deformations. Knowing the internal loads is the easiest task, but extracting the generalized deformation is not straightforward. Usually, to do so, the blade reference axis displacements and rotations are computed from the nodal displacements and rotations of the nodes forming the cross section. The longitudinal distribution of these reference axis displacements is then derived using Eq. 3 to compute the generalized deformations.

The method proposed here is highly inspired by Malcolm et al.[1]. The particularity of the proposed method is that the computation of cross-sectional displacements and rotations are performed using a formulation similar to an interpolation element like NASTRAN's RBE3 element.

The procedure to compute the distribution of cross-sectional properties along the blade length (illustrated in Fig. 9) is as follows:

1. The blade is subjected to a set of linearly independent loads cases. N load cases are needed for a $N \times N$ cross-sectional stiffness matrix.

2. n stations where the cross-sectional properties are to be computed are determined.

3. For each of these stations, the displacements (translation and rotation) of the reference point is computed using the kinematic relation linking the reference node to the connected nodes of a RBE3 element. The reference node of the element is the point that is located at the intersection of the beam's reference axis and cross-sectional plane. The connected nodes are all the nodes within a given distance on both sides of the cross-sectional plane. This distance should be as small as possible (but large enough to get nodes to cover the entire cross section) to get a good representation of the transverse shear strains.

4. Once the displacements of the beam's reference axis are known at each stations along its length, Eq. 3 is used to compute the generalized strains at each station. The derivatives are computed using second order numerical derivations on 3 points.

5. For each station, the cross-sectional stiffness matrix is computed by solving the fol-

FIG. 9. Model 4: Procedure for the cross-sectional properties evaluation from a 3D finite element model from a set of unit loads at blade tip

lowing system:

$$\begin{bmatrix} \begin{bmatrix} V_x \\ V_y \\ N \\ M_x \\ M_y \\ M_z \end{bmatrix}_1 & \dots & \begin{bmatrix} V_x \\ V_y \\ N \\ M_x \\ M_y \\ M_z \end{bmatrix}_6 \end{bmatrix} = \mathbf{K}_s \begin{bmatrix} \begin{bmatrix} \gamma^0_{zx} \\ \gamma^0_{zy} \\ \epsilon^0_z \\ \kappa_x \\ \kappa_y \\ \kappa_z \end{bmatrix}_1 & \dots & \begin{bmatrix} \gamma^0_{zx} \\ \gamma^0_{zy} \\ \epsilon^0_z \\ \kappa_x \\ \kappa_y \\ \kappa_z \end{bmatrix}_6 \end{bmatrix} \tag{51}$$

where the index of a vector designates the load case to which it is associated.

F. Application to the experimental cross-sectional analysis

The method used to compute the blade cross-sectional properties of model 4 can also be used for the evaluation of the cross-sectional properties of a blade during a bending test. As described in Section II, this test has been performed on the WESNet blade. Instead of using the displacements of connected nodes to compute the cross-sectional generalized deformations, the displacements of the 3D scanner's reflective target were used.

Only 3 modes of deformation were considered in this analysis: flapwise bending, edgewise bending and torsion. Then, the following system has to be solved to get a 3×3 stiffness matrix:

$$\begin{bmatrix} \begin{bmatrix} M_x \\ M_y \\ M_z \end{bmatrix}_1 & \dots & \begin{bmatrix} M_x \\ M_y \\ M_z \end{bmatrix}_3 \end{bmatrix} = \mathbf{K}_s \begin{bmatrix} \begin{bmatrix} \kappa_x \\ \kappa_y \\ \kappa_z \end{bmatrix}_1 & \dots & \begin{bmatrix} \kappa_x \\ \kappa_y \\ \kappa_z \end{bmatrix}_3 \end{bmatrix} \tag{52}$$

The 3 load cases used was a flapwise force near the blade tip, an edgewise force near the blade tip and an excentric force close to the blade tip (coupled torsion and flapwise bending).

G. Summary of model capabilities

To conclude this section, Table III presents a summary of the capabilities of the 4 structural models described above.

TABLE III. Summary of model capabilities

Analysis types	Model 1: beam model; cross section idealized as two rectangular strips	Model 2: beam model; strength of materials theory for thin-walled composite beams	Model 3: beam model; thin-walled cross-sectional finite elements	Model 4: shell finite element model of the whole blade
Cross-sectional properties	Local flapwise bending	Extension, two-plane bending, and their couplings; torsion	Full 6×6 cross-sectional stiffness matrix	Full 6×6 cross-sectional stiffness matrix
Natural frequencies	No	Edgewise and flapwise modes for Euler beam	Eigenvalue solution for Timoshenko beam finite elements	Eigenvalue solution for 3D shell finite elements
Deflection	No	Edgewise and flapwise deflection for Euler beam	Beam axis displacements and rotations for Timoshenko beam finite elements	Full field displacements and rotations for 3D shell finite elements
Strains	Longitudinal strain	Longitudinal strain due to extension and bending, shear strain due to torsion	Full 3D strains	Full 3D strains
Buckling	No	Linear buckling of long plates	Not implemented	Linear buckling
Strength	Based on longitudinal strain	Based on longitudinal strain	Based on fiber direction stress	Based on fiber direction stress

IV. COMPARISON OF DIFFERENT WIND TURBINE BLADE MODELS AGAINST EXPERIMENTAL RESULTS

The four different structural models presented in the previous section are now compared with each other and with the WESNet blade experimental results. First, the characteristics of each model as well as the resulting cross-sectional properties are presented. Then, the results with respect to modal analysis, deflection, strains, buckling and composite strength are discussed.

A. Models description

The simple model (model 1) of the WESNet blade is built by evaluating the local flapwise moment of inertia I (using Eq. 26) and local flapwise bending stiffness EI. These characteristics are given at each blade longitudinal station of Table I as well as at other points of interest like ply drops.

The classical strength of materials model (model 2) is used to compute the WESNet blade cross-sectional properties at the same longitudinal stations as the model 1. Each of these longitudinal station is discretized using 100 (for circular sections) to 210 (for airfoil sections) segments.

The WESNet blade is also modelled using the cross-sectional finite element method (model 3). Each section is discretized using 100 to 117 quadratic elements (depending on whether the shear web is present or not). The aerodynamic surface elements use the offset node option, i.e., the nodes are on the exterior surface of the blade and the element thickness is built towards the blade interior. The shear web elements use the conventional mid thickness surface definition. The blade cross-sectional properties are computed at the same longitudinal stations as for models 1 and 2.

The 3D shell finite element model (model 4) of the blade is built using the Altair HyperWorks suite. Hypermesh, Optistruct and Hyperview are used respectively as pre-processor, solver and post-processor. The OptiStruct solver uses the same input format as NASTRAN. The model uses 4-node linear shell elements. As seen in Figure 10, the blade is discretized with 38 elements along its chords length and the element size reduces towards the blade tip to keep their aspect as square as possible. The model uses a total of 46 763 nodes and

FIG. 10. Mesh of the WESNet 3D shell finite element model

47 272 elements (all but 3 are quadrilateral). Laminates are defined using the PCOMPP method of OptiStruct. As for the cross-sectional finite element model, nodes are on the blade's exterior surface and the element thickness is built towards the blade interior. The shear web elements use the conventional mid thickness surface definition. With this 3D shell finite element model, the methodology presented earlier is used to compute the cross-sectional properties of the WESNet blade. 75 equally spaced computation points are used along the blade length.

Using the methodology presented for model 4, the experimental WESNet blade cross-sectional properties are also computed. As the test jig does not allow the application of axial load cases and as the precision of the measurements do not allow the computation of transverse shear deformation, a 3×3 cross-sectional stiffness matrix is obtained (torsion and two axes of bending). The cross-sectional characterization test was performed on one blade only.

B. Cross-sectional properties

The cross-sectional stiffness properties computed from the different models of the WESNet blade are now compared. Due to the blade configuration, for which there are no significant couplings at the laminate level, the blade cross-sectional stiffness matrix should take the following form:

$$\mathbf{K}_s = \begin{bmatrix} K_{s11} & K_{s12} & 0 & 0 & 0 & K_{s16} \\ K_{s12} & K_{s22} & 0 & 0 & 0 & K_{s26} \\ 0 & 0 & K_{s33} & K_{s34} & K_{s35} & 0 \\ 0 & 0 & K_{s34} & K_{s44} & K_{s45} & 0 \\ 0 & 0 & K_{s35} & K_{s45} & K_{s55} & 0 \\ K_{s16} & K_{s26} & 0 & 0 & 0 & K_{s66} \end{bmatrix} \tag{53}$$

There is coupling between extension and bending because the reference axes are not necessarily centered at the elastic center (K_{s34} and K_{s35} terms) nor aligned with the principal axes of bending (K_{s45} term). There is also coupling between both transverse shear deformation (K_{s12} term). Finally, there is a coupling between the transverse shears and the torsion deformations because the reference axes are not necessarily centered at the shear center (K_{s16} and K_{s26} terms).

Models 3 and 4 are able to evaluate all the terms of the 6×6 cross-sectional stiffness matrix. Model 2 only evaluates those associated with the extension, bending and torsion deformations (K_{s33}, K_{s44}, K_{s55}, K_{s34}, K_{s35}, K_{s45} and K_{s66}). Model 1 only evaluate the local flapwise bending stiffness (K_{s44}, when the x are is the flapwise principal axis of bending). Finally, the experimentations allow computing terms associated with the bending and torsion behaviour only (K_{s44}, K_{s55}, K_{s45} and K_{s66}).

The terms of the cross-section stiffness matrix that should be null are effectively null when computed by model 3. Model 4 returns values that are not null but are small when compared to the other terms.

The detailed results for each of the non-null terms are then presented. Figure 11a, b and c present the results obtained for the terms associated with the transverse shear deformation. We can see that both models show the same trends but a significant error is observable. This is caused by the imprecision of model 4 to evaluate transverse shear properties. This imprecision is due to the fact that transverse shear deformation is small in this blade and hard to capture with the used method so a small error results in a larger relative difference.

As shown in Figure 11d, the axial stiffness from models 2, 3 and 4 are similar in the outboard region of the blade. In the inboard region, model 4 shows the same trends but with important differences. This is due to the fact that this model (3D shell finite element) is able to take into account the effects of the rapidly changing cross section shape in this part of the blade. On their side, models 2 and 3 suppose a constant cross-sectional shape. The same conclusion can be made when looking at the bending stiffness of Figure 11e and f.

As the tests performed do not include axial loads on the blade, the extension-bending couplings cannot be evaluated. So, the results of models 2, 3 and 4 have to be transferred to the elastic center to be compared with the experimental results. This is shown in Figure 11g and h where we can see a difference between the models of up to 30 % for the flapwise bending stiffness (K_{s44}) and of up to 20 % for the edgewise bending stiffness (K_{s55}). Note that the experimental results were not available for approximately the first 1 m closest to the blade root.

Starting from the cross-sectional stiffness matrices computed at the elastic center, it is

Accepted to J. Renew. Sustain. Energy 10.1063/5.0087613

possible to compute the orientation of the principal axes of bending. The results of the angle θ_1 between the x-axis and the flapwise principal axis of bending (or local flapwise axis) are shown in Figure 11i. All models return values close to each other. Transferring the K_{s44} term to this axis allows to compare with the local flapwise bending stiffness obtained from model 1. As shown in Figure 11j, model 1 return values that are close to those of the other models in the outboard region of the blade. In fact, model 1 computes values that are approximately 2 to 3 % smaller than those of the other models. A higher difference is observed from blade root to $z = 1$ m. This is because, in that region, the aerodynamic shells outside the spar caps are as thick as the spar cap, contributing to the blade stiffness, which is not taken into account in model 1. However, we can say that model 1 gives conservative results that are close to the values obtained from the other models.

The results of torsional stiffness are presented in Figure 11k, where they are transferred to the shear center for models 3 and 4 in order to be able to compare with model 2 and the experimental results. The results from models 2, 3 and 4 show similar trends. Around $z = 0.5$ m, Model 4 differs from the two others. This is due to the fact that this model takes into account the changing cross-sectional shape. When zooming in the outboard section of the blade (see Figure 11l, we can observe differences between the different models of up to 50 %. At the opposite of what was observed for bending, model 4 underestimates the torsional stiffness. This can be explained by the difficulty of obtaining good results for torsion from a shell finite element model using offset shells as reported in the literature[25–27].

As shown in Figures 11l and 11m, the shear center position as computed by models 3 and 4 are quite different. However, theses differences are still small relative to the cross-sectional dimensions. It illustrates the difficulties associated with the computation of the transverse shear properties using the 3D shell finite element model.

Results for the K_{s16}, K_{s26}, K_{s34}, K_{s35} and K_{s45} terms are not presented here as they are used to compute the elastic and shear center as well as the orientation of the principal axes of bending.

Comparing the blade cross-sectional properties from the different numerical models against the experimental data leads to the following observations. Model 1 gives a conservative but fair estimation of the local flapwise bending properties at low calculating cost. Model 2 gives very good results for extension, bending and torsion. Model 3 seems to be the most reliable according to the validation performed on it[3]. Model 4 gives very good results

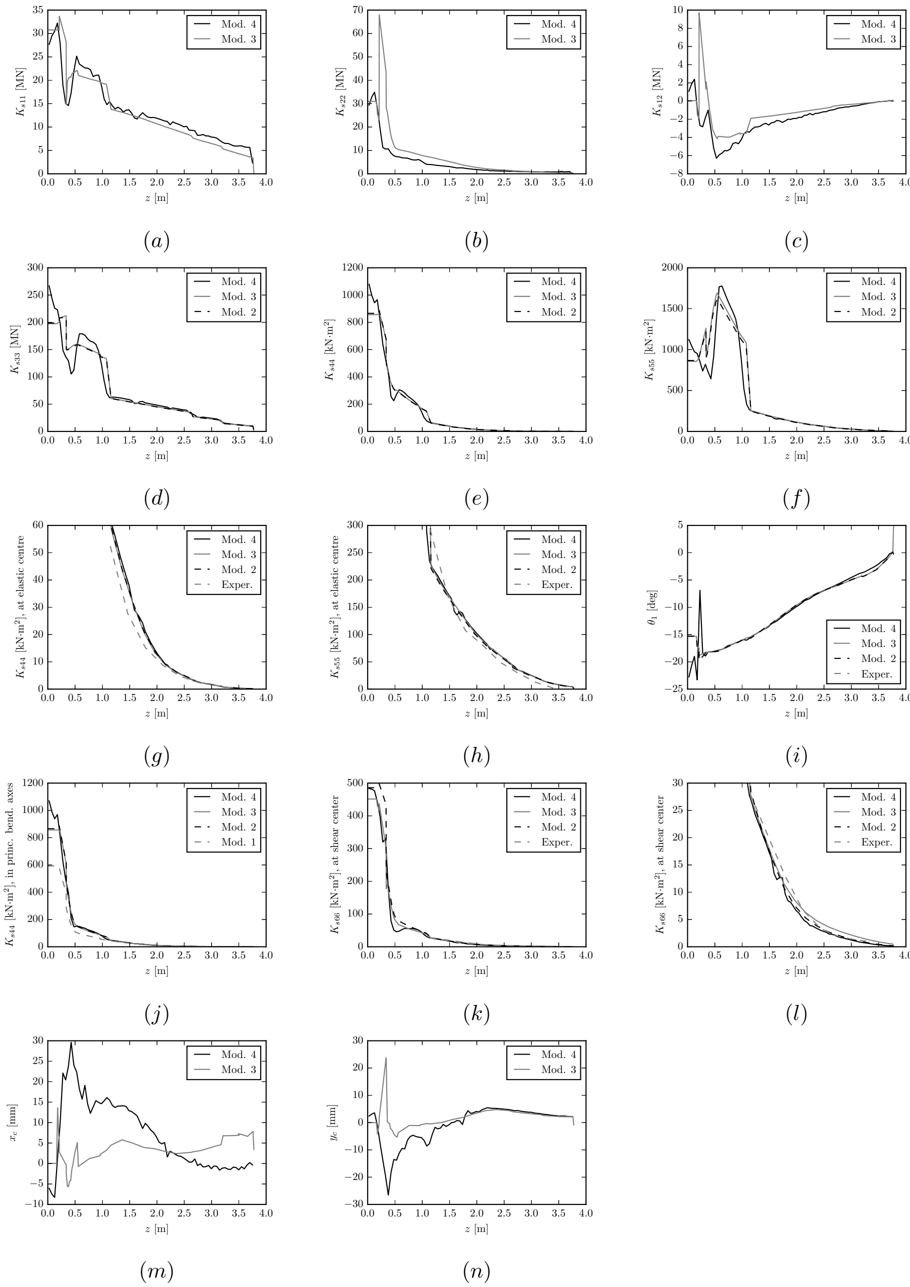

FIG. 11. Cross-sectional stiffness terms and associated properties. Experimental results come from blade 1. (a) K_{s11}. (b) K_{s22}. (c) K_{s12}. (d) K_{s33}. (e) K_{s44}. (f) K_{s55}. (g) K_{s44} at elastic centre. (h) K_{s55} at elastic center. (i) θ_1. (j) K_{s44} in principal bending axes. (k) K_{s66} at shear center. (l) K_{s66} at shear center (zoom). (m) x_c. (n) y_c

for axial and bending behaviours. For a wind turbine blade with no bend-twist coupling, models 2, 3 and 4 are correct. Model 1 is usable for preliminary analysis based on flapwise bending behaviour.

C. Natural frequencies

Blade natural frequencies computed using models 2, 3, and 4 are now compared with the experimental data. The experimental method consists in deflecting the blade tip and then, releasing it suddenly. The Fourier transform of the time-domain signal of one of the strain gauges is computed to obtain the natural frequency. Two natural frequencies can clearly be identified at 6.4 Hz and 15.0 Hz. Both blades tested give the same results.

Table IV shows the comparison of model data with experimental data. In each model, the materials' density was adjusted to get a blade mass of 21.6 kg, equivalent to the real blade. This mass does not include the 6.40 kg of steel parts at blade root. Each of these models predict a similar center of gravity location, but these values are approximately 3 % lower than the one of the real blade. For the first blade natural frequency, all three models are within 3.5 % difference relative to the experimental value. This difference increases up to 14.6 % for the second natural frequency. The differences between models 2, 3 and 4 are within a 2 to 3 % range and they are satisfactorily predicting the experimental data.

As we can see in Figure 12 for mode 3, each model predicts mode shapes that are similar to each other. Mode shapes computed by model 4 are also similar.

D. Deflection

Looking now at the blade deflections during the design load test (defined in Section II), we can see in Figure 13 that all models predict well the flapwise deflection. At tip, all values are within a 5 % interval. The experimental data were obtained from tests on two different blades (results for both two blades are shown in Figure 13). For the edgewise deflection, we can observe some scatter in the experimental data, which is normal due to the low deflection values and to the precision of the method used to compute them (see Section II).

Accepted to J. Renew. Sustain. Energy 10.1063/5.0087613

TABLE IV. Results of the blade modal analysis. m is the blade mass, Z_{cg} is the distance from its root to its center of gravity along its length and f_i is the ith blade natural frequency. δ_j is the relative difference (in %) between model j and experimental data. Experimental results are the same for both blades.

		Experimental	Model 2	Model 3	Model 4	δ_2	δ_3	δ_4
m	[kg]	21.60	21.60	21.60	21.60	0.0	0.00	0.00
Z_{cg}	[m]	1.180	1.143	1.143	1.140	-3.1	-3.1	-3.4
f_1	[Hz]	6.400	6.616	6.474	6.559	3.4	1.2	2.5
f_2	[Hz]	15.00	17.19	17.05	16.72	14.6	13.7	11.5
f_3	[Hz]	-	20.86	20.32	20.21	-	-	-
f_4	[Hz]	-	42.69	40.42	40.55	-	-	-
f_5	[Hz]	-	58.32	57.08	56.18	-	-	-

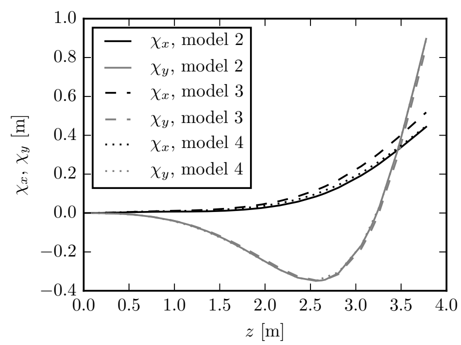

FIG. 12. Comparison of the 3rd blade mode shape. χ_x and χ_y are respectively the edgewise and flapwise deflections

E. Strains

All four models allow computing the blade strains. Figure 14 shows the maximum and minimum longitudinal strains computed over the blade length by these four models for the design load (defined in Section II). In addition to these data, the experimental results from the two blades tested are shown. The strain gauges were placed on the upper and lower

Accepted to J. Renew. Sustain. Energy 10.1063/5.0087613

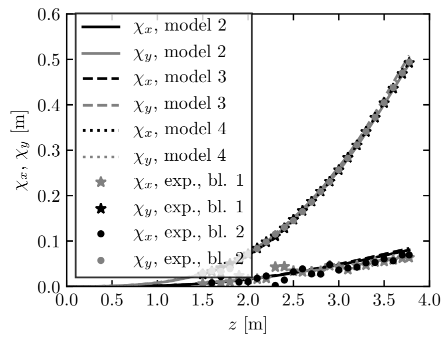

FIG. 13. Comparison of experimental and models blade deflection under the design load. χ_x and χ_y are respectively the edgewise and flapwise deflections

blade surface at 30 % of the chord length (which correspond to the chordwise blade reference axis location). As seen in Figure 14, models 2, 3 and 4 predict the strains obtained from the experiments relatively well (within a 10 % range). As expected and desirable, model 1 gives a conservative evaluation of the strain levels by overestimating them.

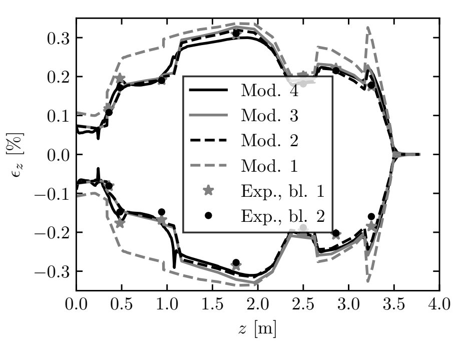

FIG. 14. Comparison of experimental and models blade strains under the design load. Top curves are lower surface data and lower curves are upper surface data

F. Buckling

During the experimentations, buckling has been observed in both steps of the destructive tests (performed on both blades tested).

During the first step (where the blade was simply supported at $z = 2360$ mm and loaded at $z = 3500$ mm), buckling was observed on the first blade tested at location $z = 2800$ mm, on the panel near the trailing edge on the airfoil upper surface. From the 3D scanner data, we know that buckling occurs between 2000 and 2250 N of load applied on the blade. When looking at the signal of the strain gauge closest to the buckling location, we can see a change in the slope at a load of 2160 N.

For the second blade tested, no buckling was observed with the 3D scanner before the blade failure under a load of 2000 N. But when looking at the signal of the strain gauge closest to the buckling location (for blade 1), a change of slope is observed at a load of around 1800 N. This value corresponds to the intersection point between a line passing through the initial slope and a line passing through the final slope.

For the second step of the destructive test (where the force was applied at $z = 2360$ mm), the 3D scanner indicates that buckling occurs between 4000 N and 6000 N applied on the blade, and this is the case for both blades. Figure 15 shows the buckling of blade 1 as recorded by the 3D scanner (blade 2 is similar). As we can see, the center of the wave that has the maximum amplitude is located at $z = 1200$ mm, where a strain gauge was installed. Again, buckling occurs on the panel near the trailing edge on the airfoil upper surface of the blade. When looking at the signal of this strain gauge for both blades, we can see a change in the slope (intersection point between lines passing through the initial and the second linear parts of the curve) at a load of 4600 N for blade 1 and at a load of 5500 N for blade 2.

FIG. 15. Buckling at $z = 1200$ mm on blade 1 during the second step of the destructive test recorded by the 3D scanner

As summarized in Table V, for the first step of the destructive tests, buckling occurs at a load level between 1800 and 2160 N at a radial location $z = 2800$ mm. For the second step of the destructive tests, buckling begins at a load between 4600 and 5500 N at 1200 mm

TABLE V. Comparison of buckling results

Model	Step 1		Step 2	
	Buckling force [N]	Buckling loc., z [mm]	Buckling force [N]	Buckling loc., z [mm]
Experimental	1800–2160	2800	4600–5500	1200
Model 2	2326	2662	3702	1160
Model 4	3066	2695	6059	1135

from the blade root.

The shell finite element model of the blade (model 4) allows computing buckling loads. Figure 16 shows the first buckling mode for both steps of the destructive test. The buckling loads are 3066 N and 6059 N for the first and second steps of the destructive test respectively. These results are also presented in Table V.

(a)

(b)

FIG. 16. Buckling results from model 4. (a) step 1, (b) step 2

The only other model able to compute buckling loads is the classical strength of materials model (model 2). For the first step of the destructive test, this model predicts a buckling load of 2326 N at the section located at 2662 mm from the blade root. For the second step, buckling occurs at 1160 mm from the root at a load level of 3702 N. These results are also summarized in Table V.

When comparing the buckling results, we can first see that the buckling locations are relatively well predicted by both models. All results are within ranges of 105 mm for step 1 and 65 mm for step 2. If we compare the buckling loads, we can see that model 2 predict lower loads than model 4. However, the experimental data for step 1 show that buckling occurs at a load that is lower than the one predicted by both models. For the second step, the experimental results range between the results of models 2 and 4.

On one hand, the buckling hypothesis for model 2 is conservative. As the blade panels are curved, the flat plate assumption leads to lower buckling loads than if a solution for curved panel was used[28]. However, on the other hand, the assumption on the panel boundary conditions can be non-conservative in some case. Here, simply supported boundary conditions are used on all sides. But with the one-shear-web configuration, the trailing edge panel is supported only by the spar cap (a thicker laminate) and not by a shear web. This leads to a boundary condition that lies somewhere between a free edge and a simply supported edge, which results in less support than the model used to get the buckling load. It probably explains the fact that model 2 gives a non-conservative buckling load for step 1. For step 2, the buckling occurs at a location where the rigidity difference between the trailing edge panel and the spar cap is higher, resulting in boundary conditions that are closer to the simply supported assumption and explaining the conservative result obtained from model 2.

When looking at the results of model 4, the ratio of shell finite element buckling loads to experimental minimum buckling loads is 1.70 for step 1 and 1.32 for step 2. The differences between the experimental data and the results from the shell finite element model can be explained partly by the fact that, as seen in the previous results (frequencies, deflections, strains), the models overestimate the blade stiffness. The buckling results go in the same way. Another important aspect explaining the results of model 4 is that, as reported in the literature[20,23], finite element linear buckling analyses are non-conservative. For instance, Bergreen et al.[20] report a non-linear buckling load as low as 65 % of the linear buckling load depending on the induced imperfections. According to that, the buckling load values obtained from model 4 seems reasonable. We can also note that these buckling behaviors occur in non-structural areas and do not lead to blade failure. Finally, it is worth noting that the non-conservative aspect of the linear finite element buckling results is formalized by some standards[29,30] where a partial safety factor of 1.25 is specified when using this type of buckling analysis.

G. Composite Strength

The last object of comparison between the different blade structural models is about the blade strength. For the first step of the destructive test, both blades failed in similar ways. A compressive failure occurs in the spar cap on the upper side. For blade 1, the failure occurs for a load around 2650 N (continuous recording of the load cell data was not available so an estimate of the failure load is given) at 2760 mm from the root. Blade 2 fails at a load level

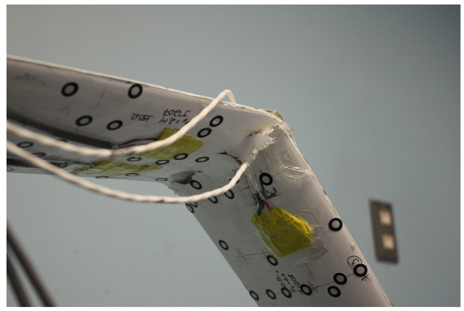

(a)

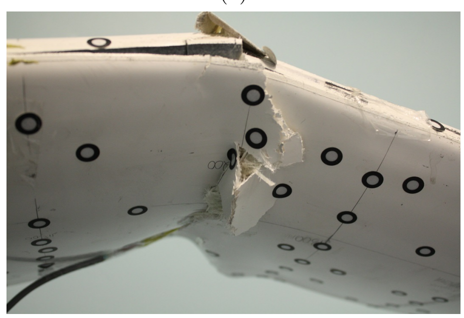

(b)

FIG. 17. Failure of blade 1 in the first (a) and second (b) step of the destructive test

of 2110 N and the failure is located at 2690 mm from the root. These values are summarized in Table VII presented at the end of this section. Figure 17a shows images of the failure of blade 1.

During the second step of the test, blade 1 fails at a load level of 10 528 N and the failure is located at 1210 mm from the blade root in the spar cap of the upper side (see Figure 17b).

The second blade fails in a different way. The failure process starts by a crack appearing on the leading edge around 450 mm from the root at a load level of 8450 N. After reaching a maximum load of 9040 N, the trailing edge suddenly opens at 700 mm from the blade root. At this moment, the load slightly decreases. After a small increase in the applied load, the blade fails at 500 mm from the root. This results in a failure of the shear web and of both upper and lower skins near the trailing edge.

As the failure process of the second blade during step 2 of the destructive test is hard to analyze with the numerical model used in this article, only the results of the first blade are used for the comparison of this section. They are reported in Table VII.

For the evaluation of the blade strength with models 1 and 2, the strength of the different laminates is needed. This is obtained by using the classical lamination theory with the following procedure as proposed in composite textbooks[13,14] :

1. The first ply failure stress is computed using the Tsai-Wu criterion.

2. For that ply, the maximum stress failure criterion is used to get the failure mode (longitudinal tension, longitudinal compression, transverse tension, transverse compression or shear).

3. If the failure mode is in the transverse direction or in shear, the stiffness dominated by the matrix properties (E_2, G_{12} and ν_{12}) are set to 0. If the failure mode is in the longitudinal direction, the stiffness dominated by the fiber properties (E_1, and ν_{12}) are set to 0.

4. This process is repeated until the maximum load is reached.

5. The failure strain is computed as the failure stress divided by the initial longitudinal modulus.

6. The failure analysis is applied to the 0° and ±45° plies only.

Table VI summarizes the tension and compression longitudinal failure strains for all laminates along the blade length. All compressive strains are lower than tensile strength.

When using the compressive failure strains within structural model 1, for the first step of the destructive test, the blade failure is predicted at $z = 3211$ mm under a force of 1288 N. A second possible failure point is located at $z = 2662$ mm and arise when the force reaches a value of 1705 N. This second failure point is interesting because it is located near the failure location observed during the tests. For the second step of the destructive test, the failure is predicted at $z = 1360$ mm under a force of 9661 N. These results are reported in Table VII.

The results obtained from structural model 2 are similar to those of model 1. For model 2, due to the asymmetry of the blade cross section, the extremum cross-sectional strains are not the same in tension and in compression. The predicted failures are in compression due to the fact that the failure strains are smaller in compression than in tension. As presented

Accepted to J. Renew. Sustain. Energy 10.1063/5.0087613

TABLE VI. Failure strains of the laminates along the blade length. e_x^T and e_x^C are respectively the tensile and compressive longitudinal failure strains

longitudinal position	e_x^T [%]	e_x^C [%]
$z < 337$ mm	1.32	0.89
337 mm $< z <$ 960 mm	1.61	1.02
960 mm $< z <$ 2624 mm	1.59	1.01
2624 mm $< z <$ 3173 mm	1.45	0.94
3173 mm $< z$	1.07	0.84

in Table VII, the predicted failures of structural model 2 are at the same locations as those of model 1, but for higher load values. So, as for the bending stiffness evaluation, model 1 gives conservative estimation of the failure load.

For models 3 and 4, the method used for the evaluation of blade failure load is based on a method described by Barbero[12]. In order to get the failure loads, all the materials' stiffnesses were given a value close to zero, except the longitudinal properties of the glass/epoxy unidirectional plies, the transverse shear of the glass/epoxy unidirectional plies and the core material properties. By doing so, the blade behaves as if transverse failures have occurred so that all the load is carried by the fibers. To avoid numerical problems associated with zero stiffness deformation modes, the transverse shear properties of the glass/epoxy unidirectional plies and the core properties were also kept unchanged. All the material strengths were set to really high values excepted the tensile and compressive longitudinal strength of the glass/epoxy unidirectional plies to force the solver to compute failure indices associated with these failure modes. The Tsai-Wu failure index F_{TW} is used. This index is the inverse of the safety factor. Note that, in this case, Tsai-Wu and maximum stress failure criterion give the same results. This gives a conservative estimation of the last ply failure strength by using a linear model.

When performing this analysis with structural model 3, for the first step of the test, a failure is predicted at $z = 3211$ mm under a force of 1452 N. Another possible failure point is located at $z = 2662$ mm and the failure occurs at a 1942 N load level. For the second step of the destructive test, a failure is predicted under a force of 11 270 N at 1360 mm from the blade root. For both steps of the test, the failure occurs in compression on the upper side's spar cap. As an example, Figure 18 shows the distribution of the composite failure index in the cross section located at $z = 1360$ mm for the second step of the destructive test under a unit load. The failure results from model 3 are presented in Table VII.

FIG. 18. Distribution of the composite failure index from model 3 (maximum value among each layer) in the cross section located at $z = 1360$ mm for the second step of the destructive test under a unit load. The inverse of the maximum failure index gives the failure load: $1/8.87 \times 10^{-5} = 11\ 270$

The failure results from model 4 are summarized in Figure 19, showing the composite failure index distribution for unit loads. For both steps, a compressive failure is predicted on the upper side of the blade. Two points are identified for both steps, they correspond to the two highest values of the failure index. The failure results of model 4 are summarized in Table VII

(a)

(b)

FIG. 19. Failure indices from model 4 (maximum value among each layer) under unit loads. The failure load can be computed as the inverse of the failure index. (a) Step 1. (b) Step 2

When comparing the results of Table VII, we can see that the failure locations are relatively well predicted by all models. Sometimes, the first failure predicted is not exactly at the experimental failure point, but a second point of high failure index is located close to the experimental failure point. The predicted failure loads are conservative or close to the observed values. As expected, the results from model 1 are the most conservative, but give very good insight on the failure behaviour despite the model simplicity. As also expected, model 4 is the most precise.

V. CONCLUSION

In conclusion, the simple model (model 1), despite its simplicity, gives fair results for the local flapwise bending stiffness, the strain distribution and the blade failure. In addition to

Accepted to J. Renew. Sustain. Energy 10.1063/5.0087613

TABLE VII. Comparison of blade strength results

Model	Step 1		Step 2	
	Failure load [N]	Failure loc., z [mm]	Failure load [N]	Failure loc., z [mm]
Experimental	2110–2650	2690–2760	10 530	1210
Model 1	1288, 1705	3211, 2662	9661	1361
Model 2	1723, 1925	3211, 2662	11 010	1360
Model 3	1452, 1942	3211, 2662	11 270	1360
Model 4	1704, 2249	3215, 2687	10 850, 13 080	1135, 1273

that, it returns conservative results. However, this model does not allow the evaluation of the blade's natural frequencies, deflection (a conservative evaluation of the deflection of the untwisted blade could be performed, but was not done here) and buckling. This model is well suited for preliminary design based on blade strength.

The classical strength of materials model (model 2) gives good results for cross-sectional properties, natural frequencies, deflection, strain and composite failure. Buckling has to be handled with care as non-conservative results are obtained despite the conservative hypothesis of the model. Also, this model is limited to blades using orthotropic laminates (i.e., no material couplings at the laminate level). Care must also be paid to the region where the shape of the cross section is varying quickly. The stress, strain and failure index are not accurate in these regions.

The cross-sectional finite element model (model 3) gives the more reliable results for the cross-sectional properties, especially for properties associated with transverse shear. This model is well suited for beams that use material coupling (bend-twist coupling for wind turbine blades for instance). It gives good results for natural frequencies, deflections, strains and composite strength, but as the classical strength of materials model, it suffers from a lack of precision in the region where the shape of the cross section is varying quickly. No buckling analysis was implemented within model 3, but it could be possible to implement something similar to model 2, with similar results.

These latter two models are well suited for more detailed design and for providing the blade cross-sectional properties needed for the aeroelastic analysis without having to build a 3D shell finite element model, which is much more time consuming.

The 3D shell finite element model (model 4) is the more precise and is the only one that can manage the regions of the blade where the cross-sectional shape changes quickly. However, it is less reliable than model 3 for the computation of cross-sectional properties associated with transverse shear. The results of the buckling analysis also have to be used with caution since they are not conservative. The 3D finite element model is the ideal model for the final validation of the blade.

When looking at the time to build and run these different models, we can say that models 1, 2 and 3 has similar build times. Both of these models require a tabular description of the blade. Assuming that the blade aerodynamic shape is known (in a tabular format), that the airfoil contour point files are available and that the material properties and layups are defined, these models can be built in minutes. As model 1 require only the informations about spar caps, it is even shorter than that. Model 4 can be built as quickly as model 2 and 3 if a tool generating finite element model from a tabular description of the blade is available. However, for the final stage of the design process, when a geometric model needs to be done using a CAD software and then, meshed, the built time increases to hours. In regards to the simulation time, models 1, 2, 3 and 4 take respectively 0.1 s, 4.5 s, 28 min and 3 min 25 s to solve two load cases on the same computer. These times include buckling analysis for models 2 and 4. It is important to note that the considerable solving time for model 3 is due to the fact it uses a fine mesh and that this in-house code uses an interpreted language (Python) and no code optimization has been done yet. Its conversion into a compiled language would reduce the simulation time.

To conclude this paper, the wind turbine blade design process presented in Figure 20 is proposed. The inner circle represents the very first stages of the design process where model 1 can be used to validate the feasibility of an aerodynamic design and get an idea of the mass distribution. A set of loads can be obtained on a standstill blade under the extreme wind model without information about the blade mass or stiffness. Once the aerodynamic design seems feasible, the process can go to the second circle. If no blade stiffness information is available, an aeroelastic model with rigid blades can be used to get the loads. Model 2 or 3 can be used to get a preliminary structural design and to compute the blade stiffness properties. The process can then enter the outer circle, where model 4 is used for the blade dimensioning and validation and where the aeroelastic model uses flexible blades.

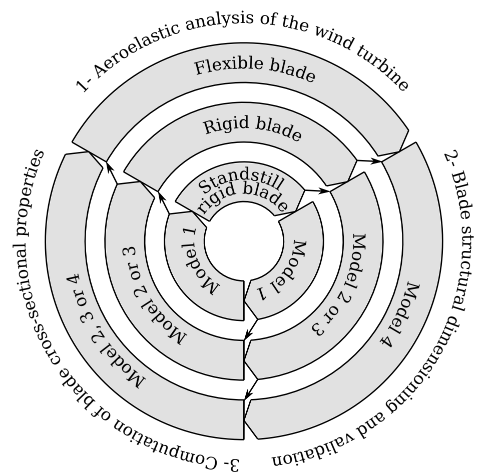

FIG. 20. Proposed wind turbine blade design process: The inner circle represents the very first stages of the design process that will evolve towards the outer circles as the blade design refines

ACKNOWLEDGEMENTS

This work was supported by the Fonds québécois de la recherche sur la nature et les technologies (FQRNT, Quebec, Canada) [Doctoral research scholarships, B2].

AUTHOR DECLARATIONS

Declaration of conflicts of interest

The authors declared no potential conflicts of interest with respect to the research, authorship, and/or publication of this article.

REFERENCES

[1]David J. Malcolm and Daniel L. Laird. Extraction of equivalent beam properties from blade models. *Wind Energy*, 10:135–157, 2007.

[2]Louis-Charles Forcier, Jon Sumner, Tommy Gagnon, Jean-François Charron, and Simon Joncas. Structural design and validation of a 10 kW wind turbine blade. In *19th Inter-*

national Conference on Composite Materials, Montréal (Québec, Canada), 28 July – 2 August, 2013.

[3]Louis-Charles Forcier. *Development and validation of tools for the structural design of wind turbine blades*. PhD thesis, École de technologie supérieure, Montréal (Canada), 2020.

[4]G. R. Cowper. The shear coefficient in Timoshenko's beam theory. *Journal of Applied Mechanics*, June:335–340, 1966.

[5]Philippe Giguère and Michael S. Selig. Blade geometry optimization for the design of wind turbine rotor. In *2000 ASME Wind Energy Symposium*, Reno (Nevada, United States), 10–13 January, 2000.

[6]B. Hillmer, T. Borstelmann, P.A. Schaffarczyk, and L. Dannenberg. Aerodynamic and structural design of multiMW wind turbine blades beyond 5 MW. In *The Science of Making Torque from Wind*, Lyngby (Denmark), 28–31 August, 28-31 août 2007.

[7]Lars P. Mikkelsen. A simplified model predicting the weight of the load carrying beam in a wind turbine blade. In *37th Risø International Symposium on Materials Science*, Roskilde (Denmark), 5–8 September, 2016.

[8]Martin O. L. Hansen. *Aerodynamics of Wind Turbines*. Earthscan, London (United Kingdom), 2nd edition, 2008.

[9]Robert M. Rivello. *Theory and Analysis of Flight Structures*. McGraw-Hill, New York (New York, United States), 1969.

[10]André Bazergui, Thang Bui-Quoc, André Biron, Georges McIntyre, and Charles Laberge. *Résistance des matériaux*. Presses internationales Polytechnique, Montréal (Québec, Canada), 3rd edition, 2002.

[11]László P. Kollár and George S. Springer. *Mechanics of Composite Structures*. Cambridge University Press, Cambridge (United Kingdom), 2003.

[12]E. J. Barbero. *Introduction to Composite Materials Design*. Taylor & Francis, New York (New York, United States), 1999.

[13]Jean-Marie Berthelot. *Matériaux composites: Comportement mécanique et analyse des structures*. Lavoisier, Paris (France), 5th edition, 2012.

[14]Ronald F. Gibson. *Principles of composite material mechanics*. CRC Press, Boca Raton (Florida, United States), 2nd edition, 2007.

[15]V. Giavotto, M. Borri, P. Mantegazza, and G. Ghiringhelli. Anisotropic beam theory and applications. *Computers & Structures*, 16(1–4):403–413, 1983.

[16]José Pedro Blasques and Mathias Stolpe. Multi-material topology optimization of laminated composite beam cross sections. *Composite Structures*, 94(11):3278–3289, 2012.

[17]José Pedro Blasques. User's Manual for BECAS : A cross section analysis tool for anisotropic and inhomogeneous beam sections of arbitrary geometry. Technical Report Risø-R-1785(EN), Risø DTU – National Laboratory for Sustainable Energy, Roskilde (Denmark), 2012.

[18]José Pedro Blasques. *Optimal Design of Laminated Composite Beams*. PhD thesis, Technical University of Denmark, Lyngby (Denmark), 2011.

[19]J. P. Blasques, R. D. Bitsche, V. Fedorov, and B. S. Lazarov. Accuracy of an efficient framework for structural analysis of wind turbine blades. *Wind Energy*, 19:1603–1621, 2016.

[20]C. Berggreen, K. Branner, J. F. Jensen, and J. P. Schultz. Application and analysis of sandwich elements in the primary structure of large wind turbine blades. *Journal of Sandwich Structures and Materials*, 9:525–551, 2007.

[21]Find Mølholt Jensen. *Ultimate Strength of a Large Wind Turbine Blade*. PhD thesis, Risø National Laboratory for Sustainable Energy and Technical University of Denmark, Roskilde and Lyngby (Denmark), 2008.

[22]Patricio Lillo. Static and fatigue analysis of wind turbine blades subject to cold weather conditions using finite element analysis, 2011. Master's thesis, University of Victoria, Victoria (British Columbia, Canada).

[23]J. A. Paquette and P. S. Veers. Increased strength in wind turbine blades through innovative structural design. In *AWEA Windpower 2008*, Houston (Texas, United States), 1–4 June, 2008.

[24]M. Tarfaoui, H. Khadimallah, A. Imad, and J. Y. Pradillon. Design and finite element modal analysis of 48m composite wind turbine blade. *Applied Mechanics and Materials*, 146:170–184, 2012.

[25]V. Fedorov and C. Berggreen. Bend-twist coupling potential of wind turbine blades. In *The Science of Making Torque from Wind 2014*, Lyngby (Denmark), 17–20 June, 2014.

[26]Kim Branner, Peter Berring, Christian Berggreen, and Henrik W. Knudsen. Torsional performance of wind turbine blades – part II: Numerical validation. In *16th International Conference on Composite Materials*, Kyoto (Japan), 8–13 July, 2007.

[27] Daniel L. Laird, Felicia C. Montoya, and David J. Malcolm. Finite element modeling of wind turbine blades. In *2005 ASME Wind Energy Symposium / 43rd AIAA Aerospace Sciences Meeting and Exhibit*, Reno (Nevada, United States), 10–13 January, 2005.

[28] C. Lindenburg and G. D. de Winkel. Buckling load prediction tools for rotor blades. mode description of tools for buckling of thin-walled beams. Technical Report ECN-C--05-103, Energy Research Center of The Netherlands, Petten (The Netherlands), 2005.

[29] Germanischer Lloyd. Guideline for the certification of wind turbines. Guideline Edition 2010, Germanischer Lloyd, Hamburg (Germany), 2010.

[30] DNV GL. Rotor blades for wind turbines. Standard DNVGL-ST-0376 Edition December 2015, DNV GL, Høvik (Norway), 2015.

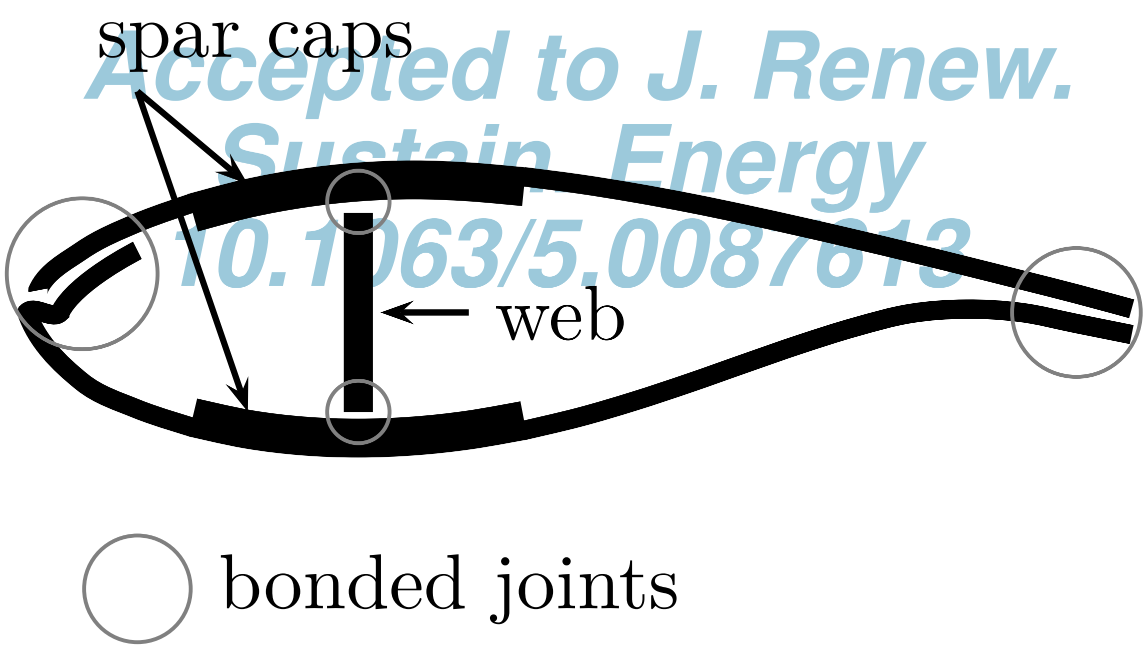
spar caps
web
bonded joints

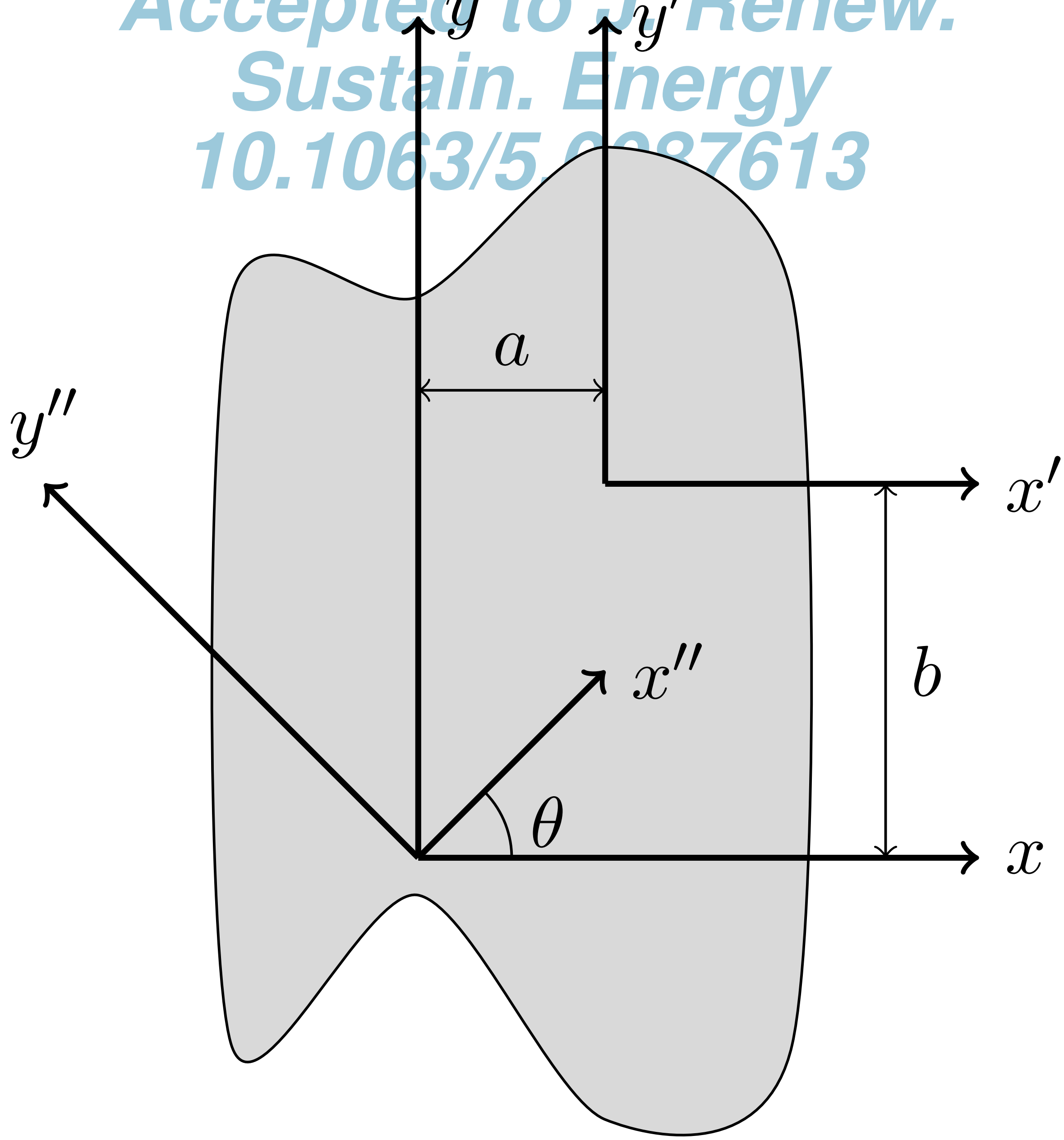

y
y'
a
y''
x'
b
x''
θ
x

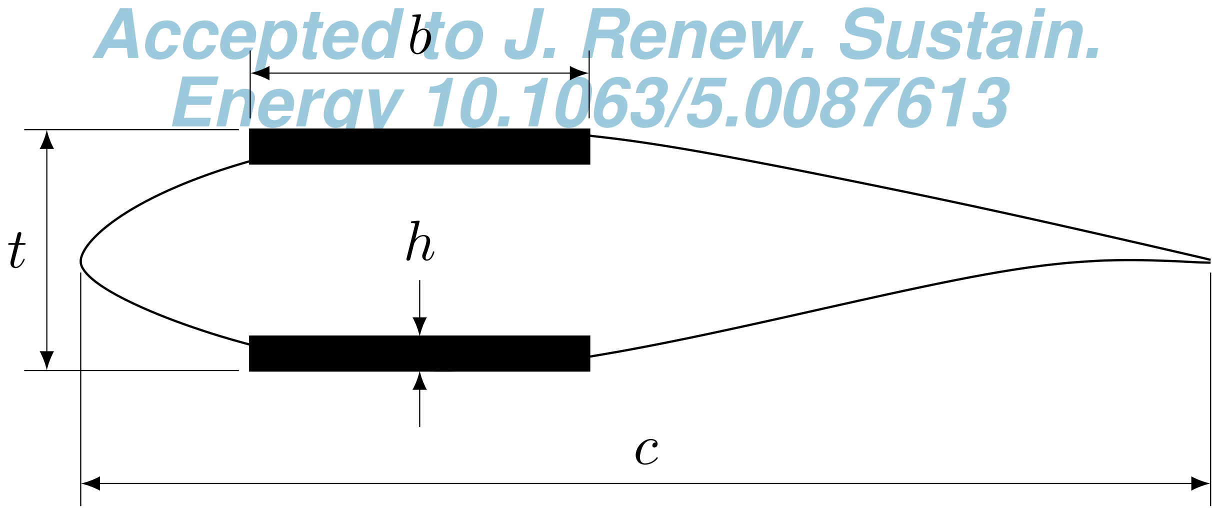
b
t
h
c

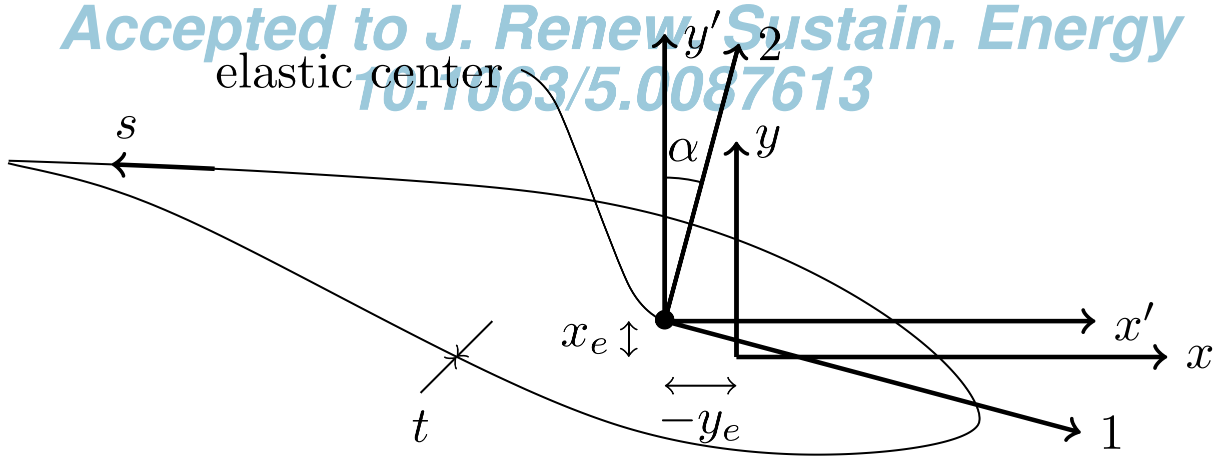
elastic center
s
t
y'
2
y
α
x'
x
1
x_e
$-y_e$

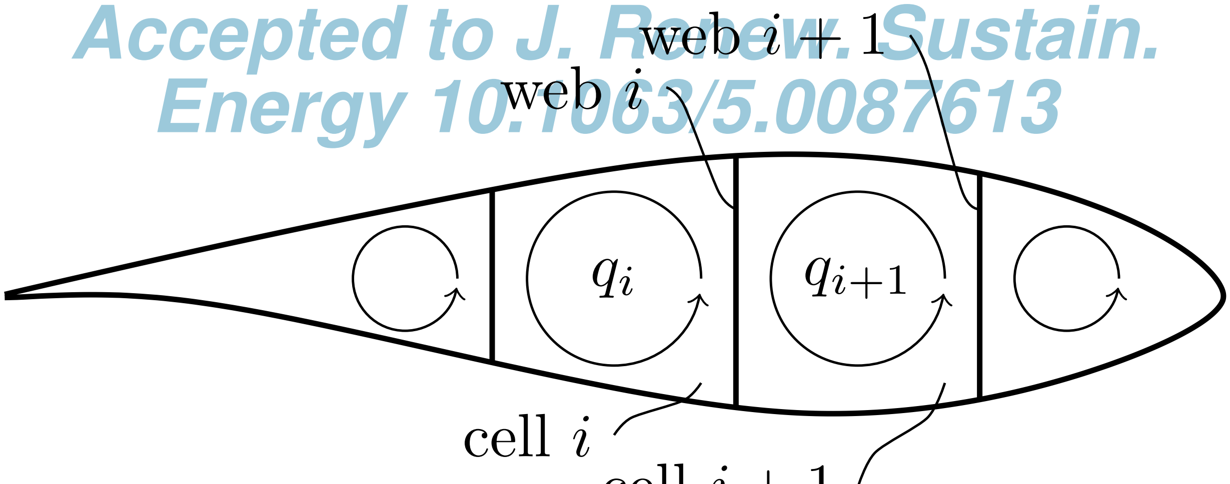
web $i+1$
web i
q_i
q_{i+1}
cell i
cell $i+1$

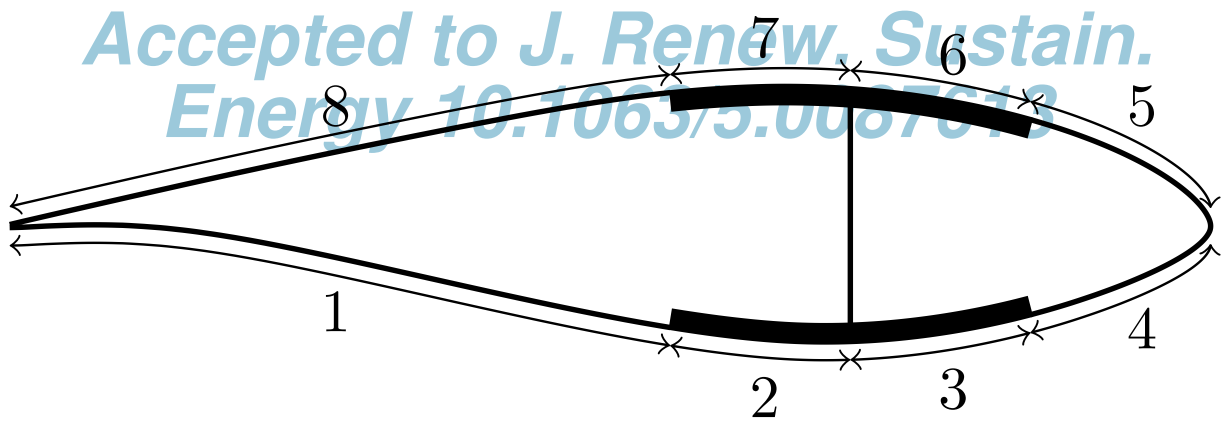
7
6
8
5
1
4
2
3

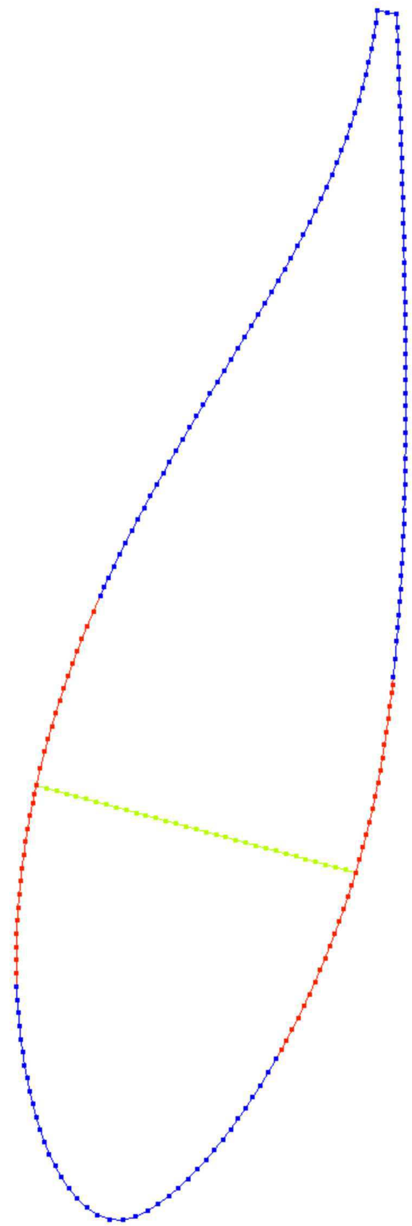

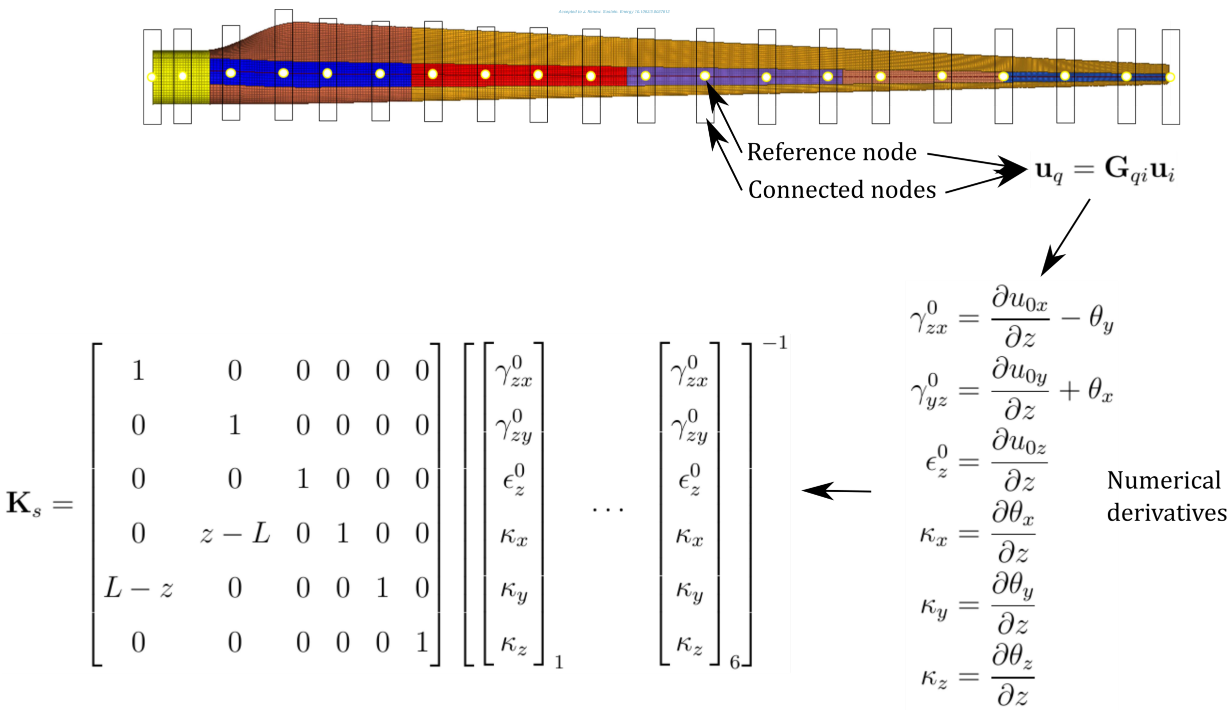
Reference node
Connected nodes
$\mathbf{u}_q = \mathbf{G}_{qi}\mathbf{u}_i$
$\gamma^0_{zx} = \frac{\partial u_{0x}}{\partial z} - \theta_y$
$\gamma^0_{yz} = \frac{\partial u_{0y}}{\partial z} + \theta_x$
$\epsilon^0_z = \frac{\partial u_{0z}}{\partial z}$
$\kappa_x = \frac{\partial \theta_x}{\partial z}$
$\kappa_y = \frac{\partial \theta_y}{\partial z}$
$\kappa_z = \frac{\partial \theta_z}{\partial z}$
Numerical derivatives
$\mathbf{K}_s = \begin{bmatrix} 1 & 0 & 0 & 0 & 0 & 0 \\ 0 & 1 & 0 & 0 & 0 & 0 \\ 0 & 0 & 1 & 0 & 0 & 0 \\ 0 & z-L & 0 & 1 & 0 & 0 \\ L-z & 0 & 0 & 0 & 1 & 0 \\ 0 & 0 & 0 & 0 & 0 & 1 \end{bmatrix} \left[\begin{bmatrix} \gamma^0_{zx} \\ \gamma^0_{zy} \\ \epsilon^0_z \\ \kappa_x \\ \kappa_y \\ \kappa_z \end{bmatrix}_1 \cdots \begin{bmatrix} \gamma^0_{zx} \\ \gamma^0_{zy} \\ \epsilon^0_z \\ \kappa_x \\ \kappa_y \\ \kappa_z \end{bmatrix}_6 \right]^{-1}$

Journal of Renewable and Sustainable Energy

ACCEPTED MANUSCRIPT

PLEASE CITE THIS ARTICLE AS DOI: 10.1063/5.0087613

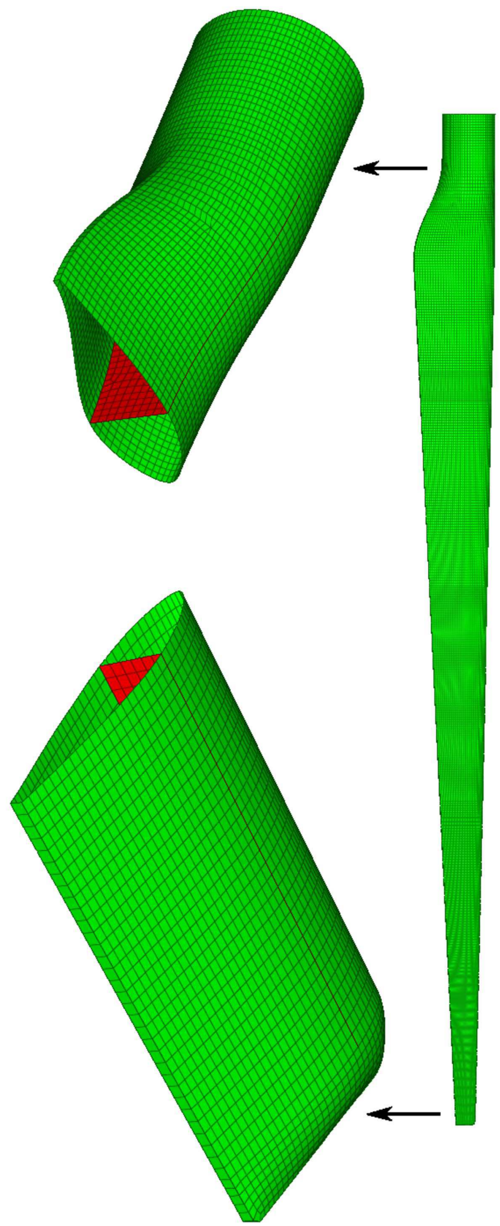

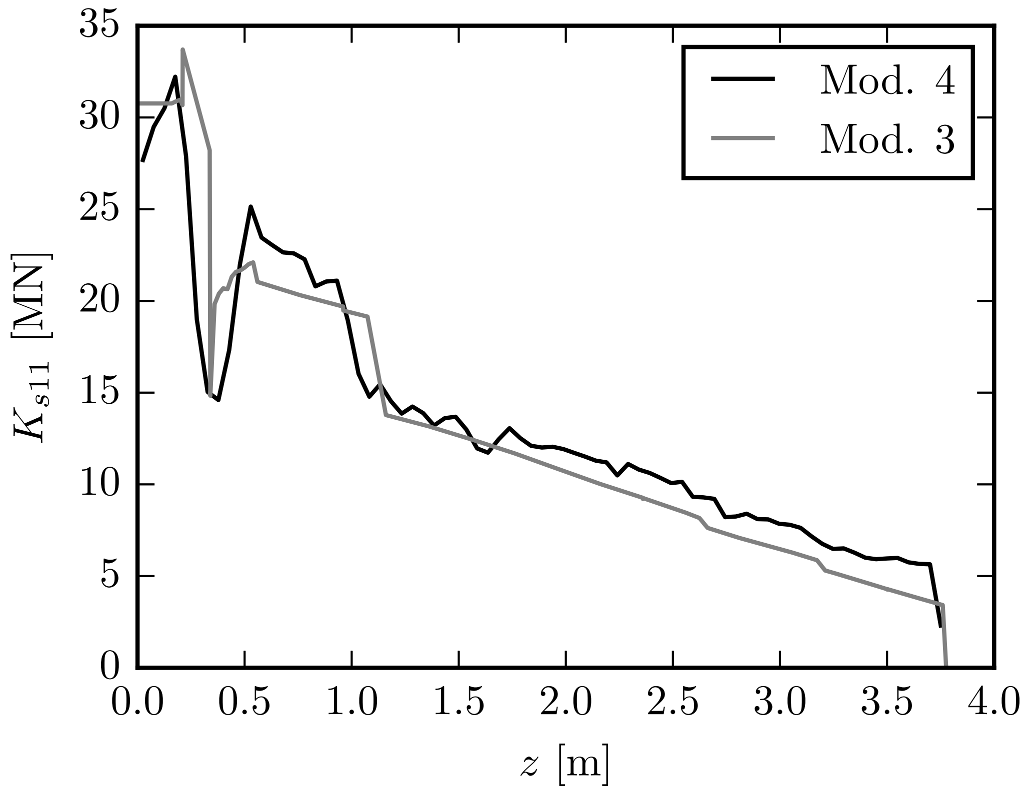
Mod. 4
Mod. 3
K_{s11} [MN]
z [m]
0
5
10
15
20
25
30
35
0.0
0.5
1.0
1.5
2.0
2.5
3.0
3.5
4.0

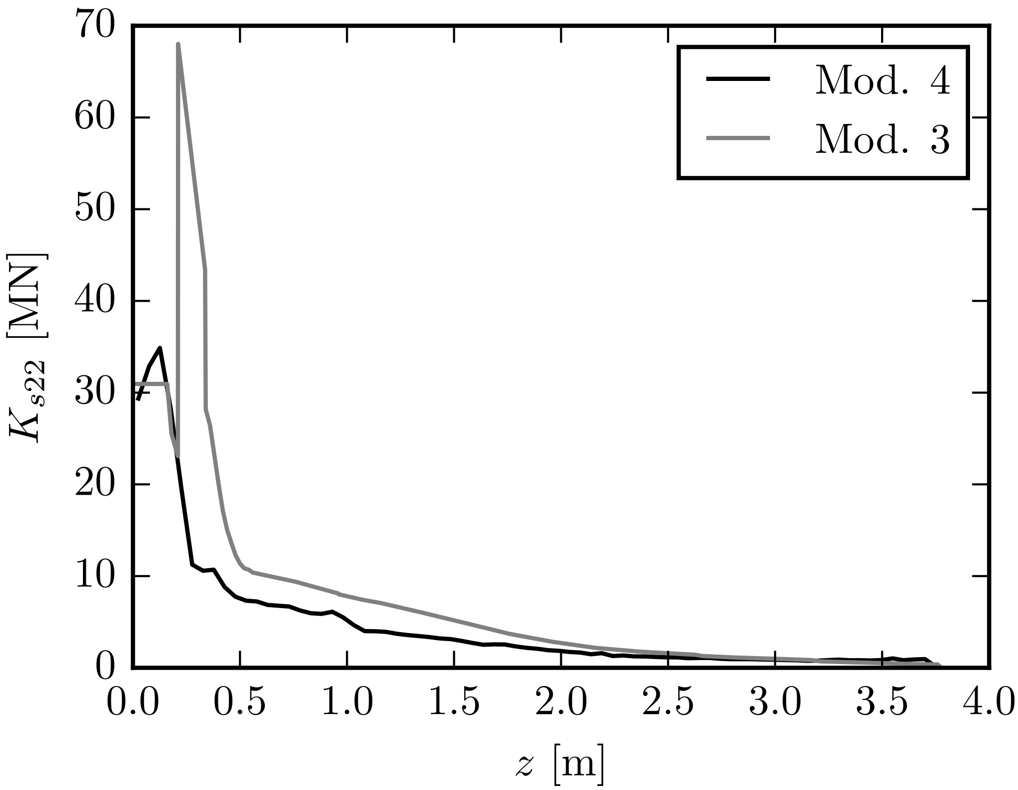
Mod. 4
Mod. 3
K_{s22} [MN]
z [m]
0
10
20
30
40
50
60
70
0.0
0.5
1.0
1.5
2.0
2.5
3.0
3.5
4.0

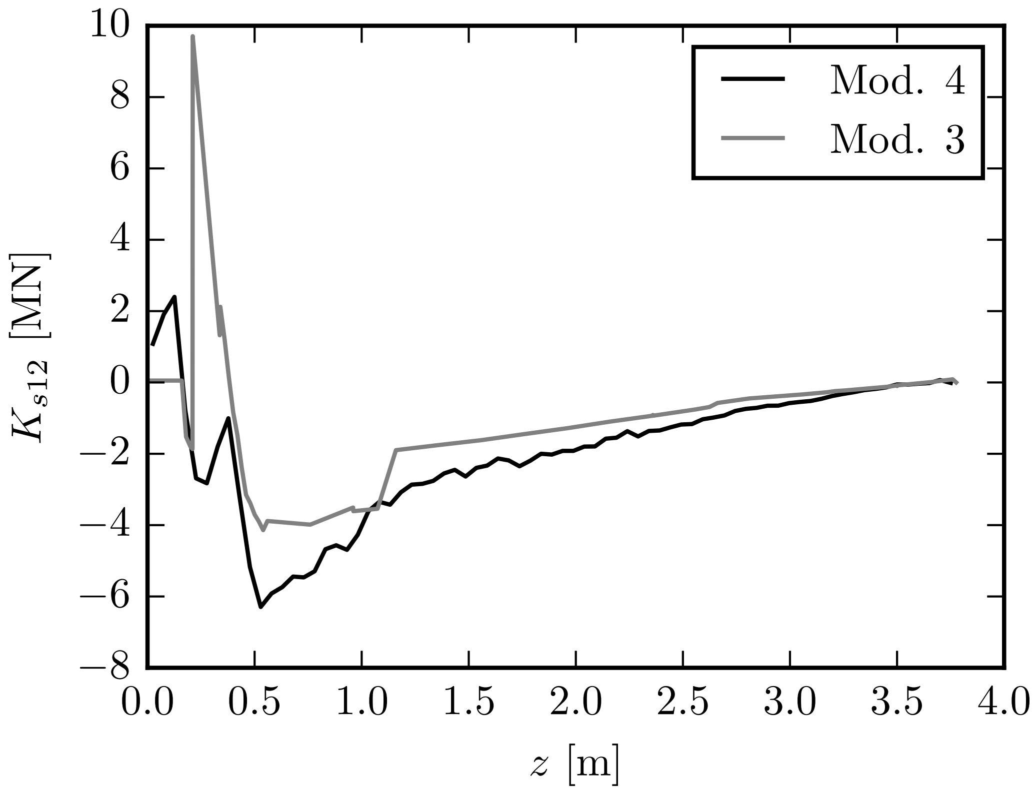
Mod. 4
Mod. 3
K_{s12} [MN]
z [m]
10
8
6
4
2
0
−2
−4
−6
−8
0.0
0.5
1.0
1.5
2.0
2.5
3.0
3.5
4.0

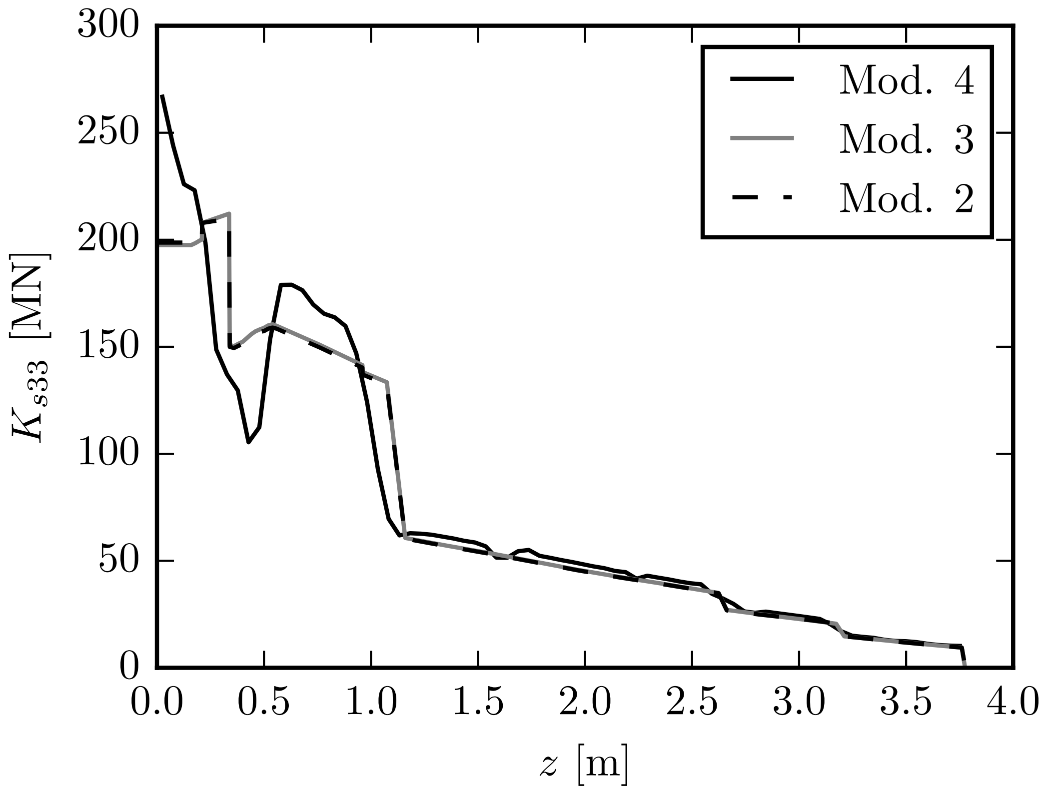
Mod. 4
Mod. 3
Mod. 2
K_{s33} [MN]
300
250
200
150
100
50
0
0.0
0.5
1.0
1.5
2.0
2.5
3.0
3.5
4.0
z [m]

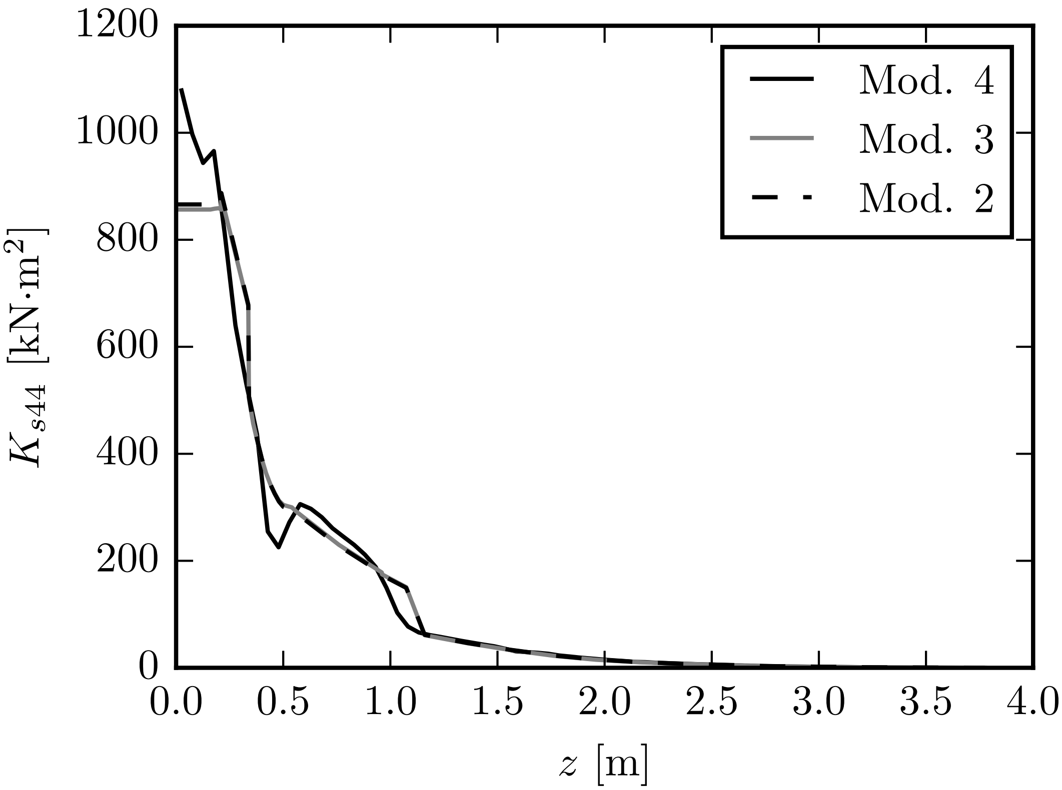
Mod. 4
Mod. 3
Mod. 2
K_{s44} [kN·m^2]
z [m]
0
200
400
600
800
1000
1200
0.0
0.5
1.0
1.5
2.0
2.5
3.0
3.5
4.0

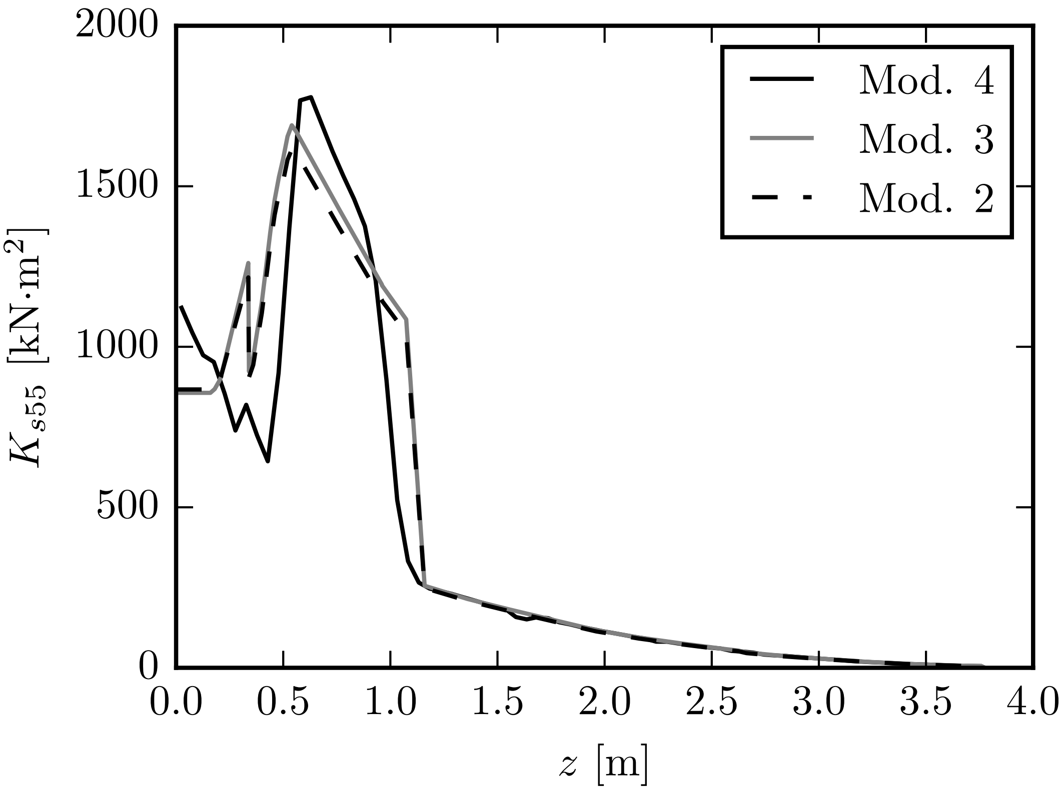
Mod. 4
Mod. 3
Mod. 2
K_{s55} [kN·m^2]
z [m]
0
500
1000
1500
2000
0.0
0.5
1.0
1.5
2.0
2.5
3.0
3.5
4.0

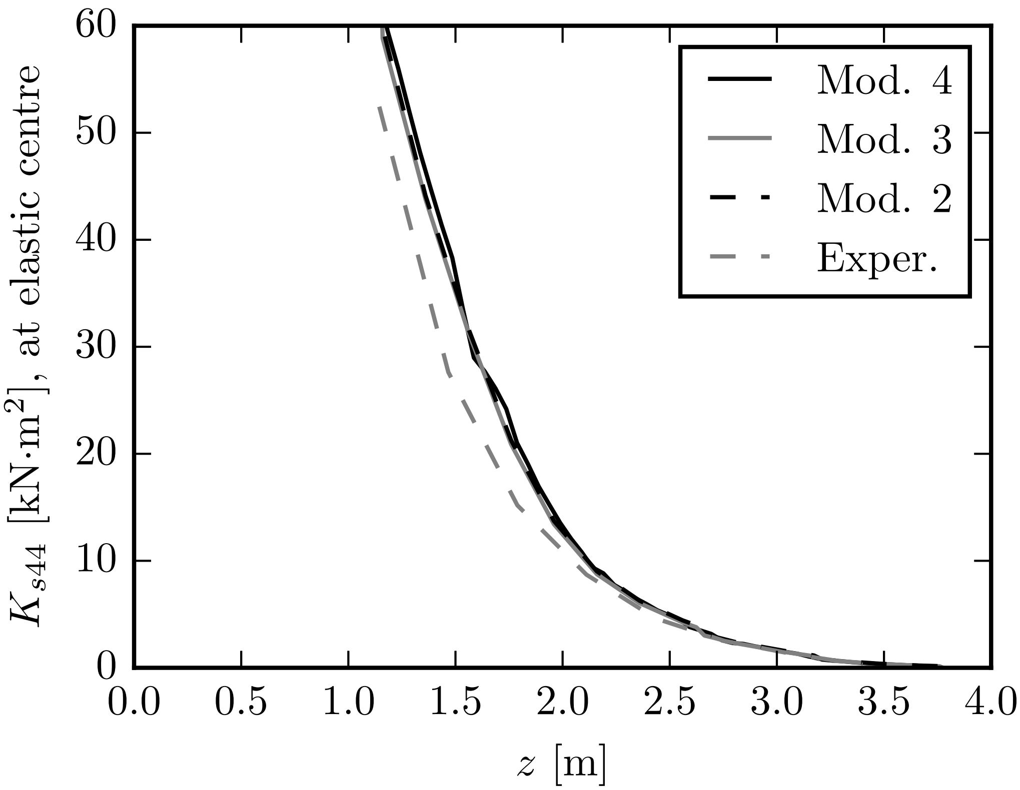
60
50
40
30
20
10
0
0.0
0.5
1.0
1.5
2.0
2.5
3.0
3.5
4.0
K_{s44} [kN·m^2], at elastic centre
z [m]
Mod. 4
Mod. 3
Mod. 2
Exper.

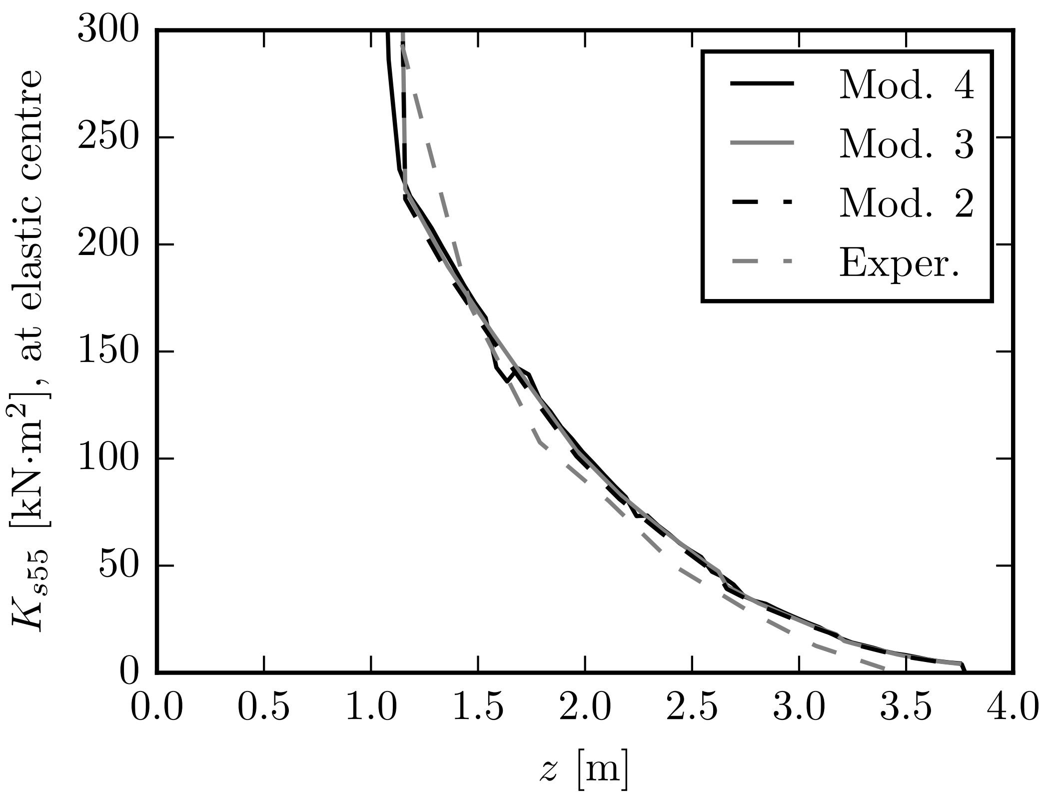
K_{s55} [kN·m^2], at elastic centre
z [m]
Mod. 4
Mod. 3
Mod. 2
Exper.
0
50
100
150
200
250
300
0.0
0.5
1.0
1.5
2.0
2.5
3.0
3.5
4.0

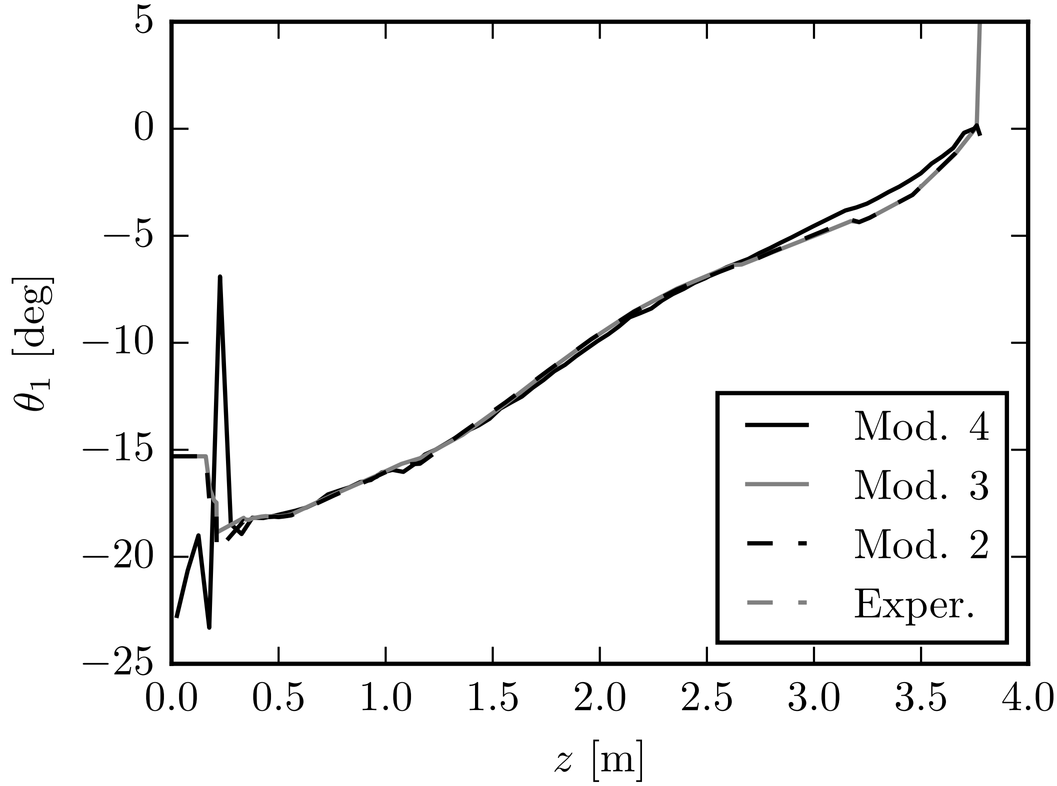
θ_1 [deg]
z [m]
Mod. 4
Mod. 3
Mod. 2
Exper.

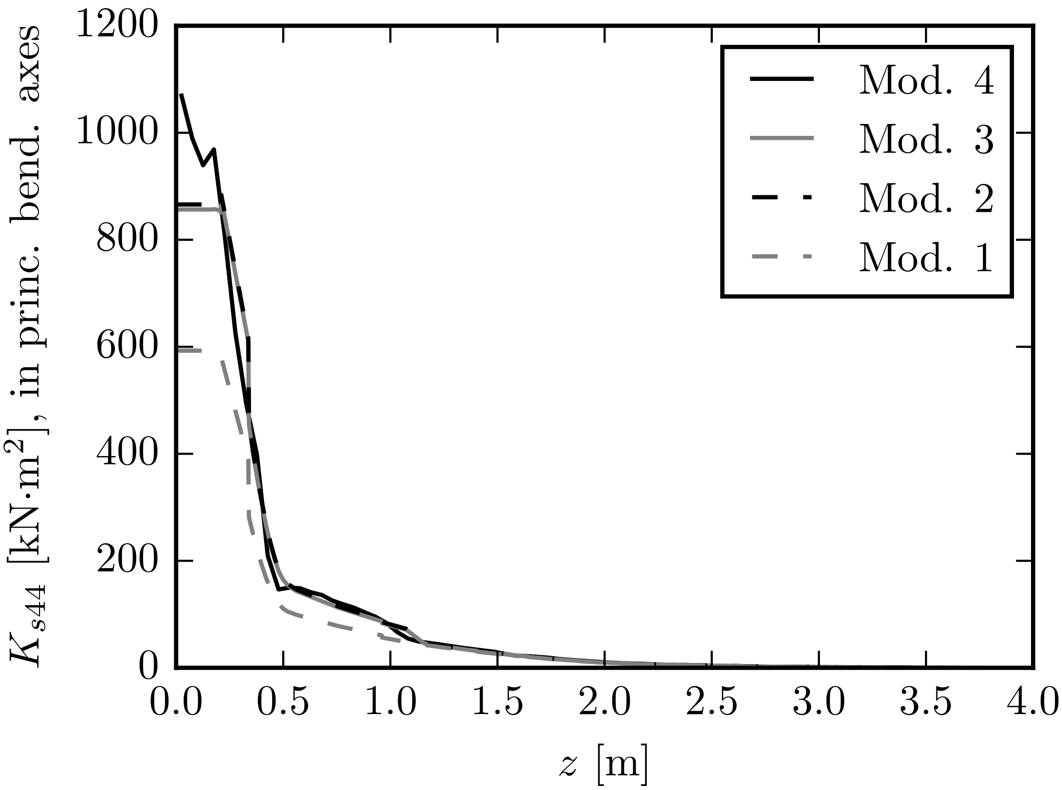
K_{s44} [kN·m^2], in princ. bend. axes
z [m]
Mod. 4
Mod. 3
Mod. 2
Mod. 1
0
200
400
600
800
1000
1200
0.0
0.5
1.0
1.5
2.0
2.5
3.0
3.5
4.0

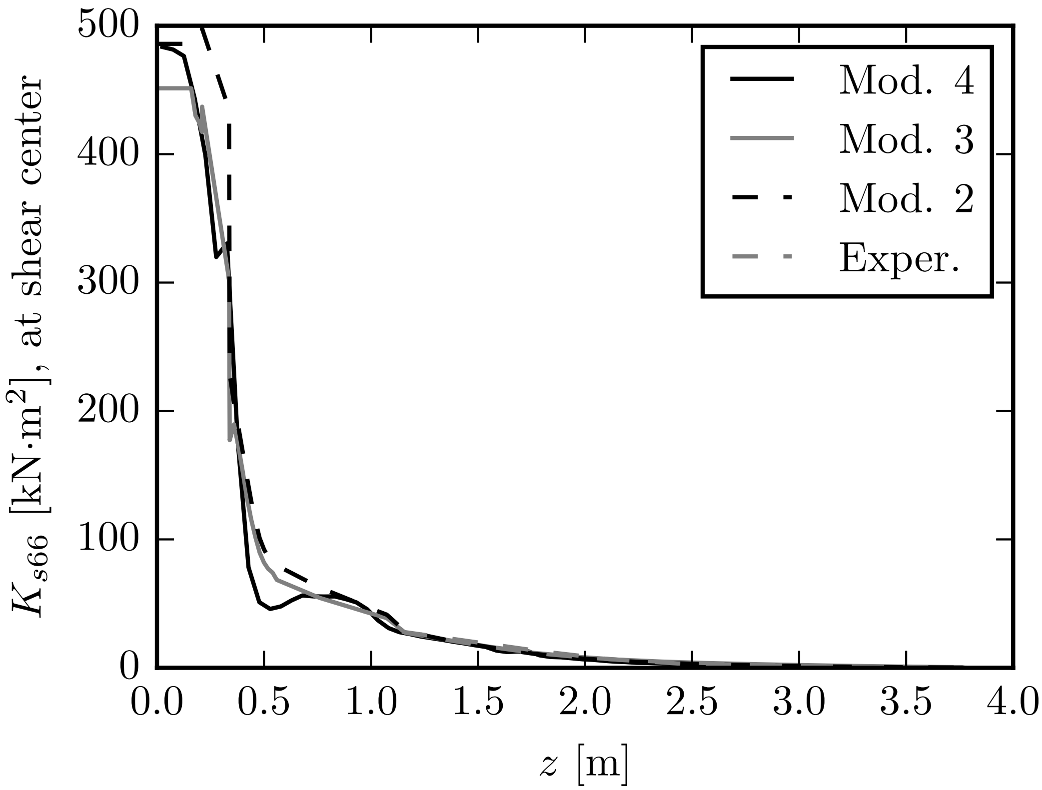
Mod. 4
Mod. 3
Mod. 2
Exper.
K_{s66} [kN·m^2], at shear center
z [m]
0
100
200
300
400
500
0.0
0.5
1.0
1.5
2.0
2.5
3.0
3.5
4.0

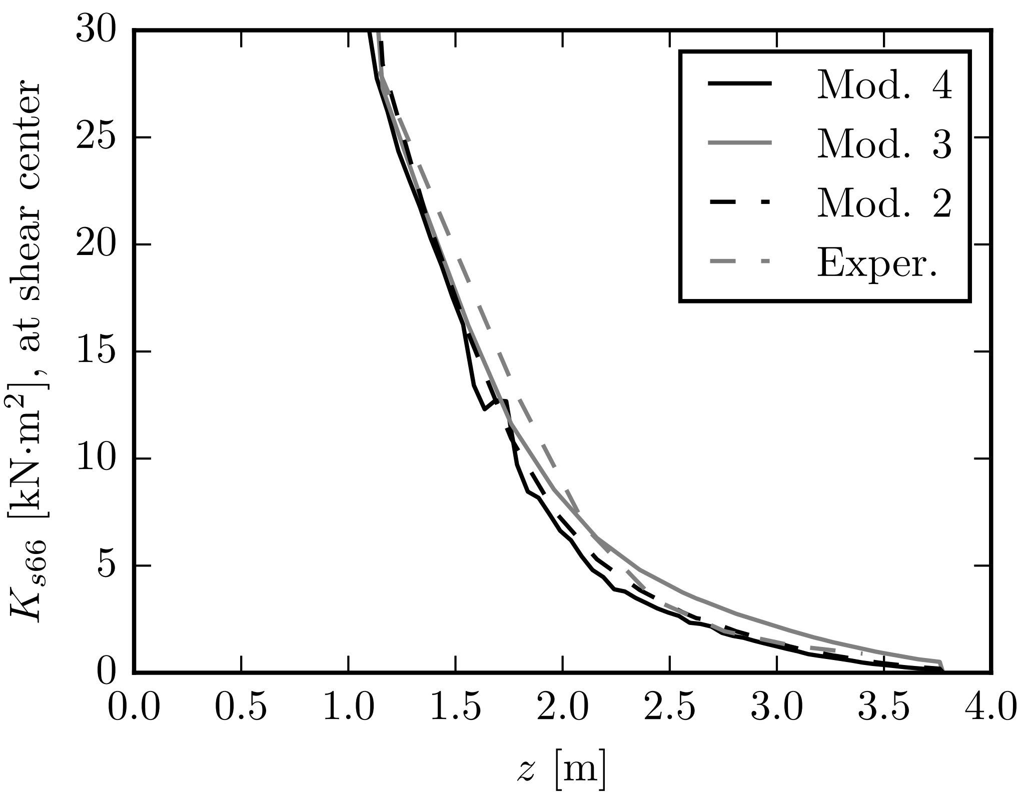
K_{s66} [kN·m^2], at shear center
z [m]
Mod. 4
Mod. 3
Mod. 2
Exper.
0
5
10
15
20
25
30
0.0
0.5
1.0
1.5
2.0
2.5
3.0
3.5
4.0

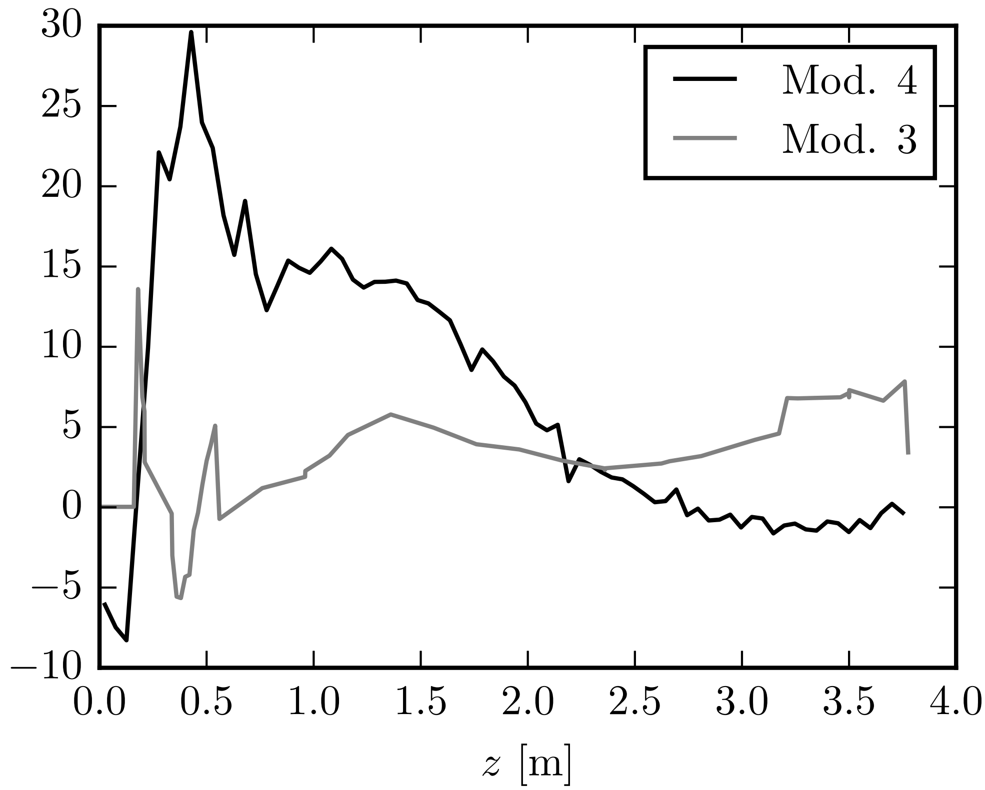
Mod. 4
Mod. 3
x_c [mm]
z [m]
30
25
20
15
10
5
0
−5
−10
0.0
0.5
1.0
1.5
2.0
2.5
3.0
3.5
4.0

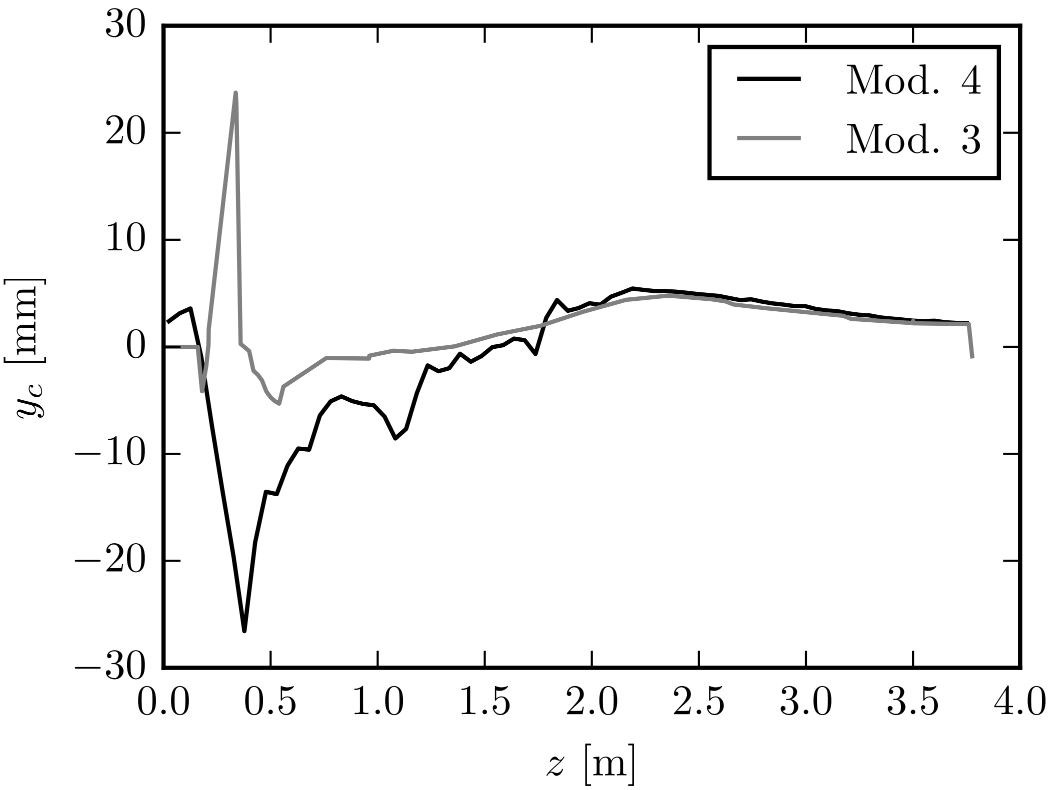
Mod. 4
Mod. 3
y_c [mm]
z [m]
30
20
10
0
−10
−20
−30
0.0
0.5
1.0
1.5
2.0
2.5
3.0
3.5
4.0

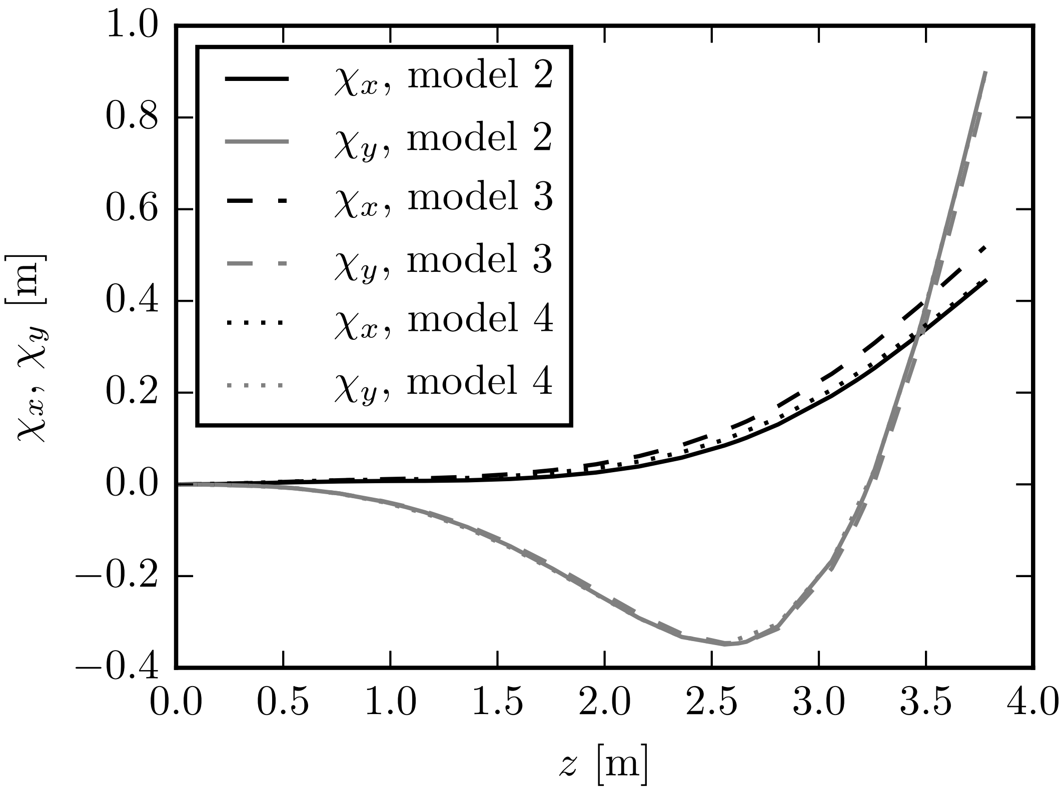
χ_x, model 2
χ_y, model 2
χ_x, model 3
χ_y, model 3
χ_x, model 4
χ_y, model 4
χ_x, χ_y [m]
1.0
0.8
0.6
0.4
0.2
0.0
−0.2
−0.4
0.0
0.5
1.0
1.5
2.0
2.5
3.0
3.5
4.0
z [m]

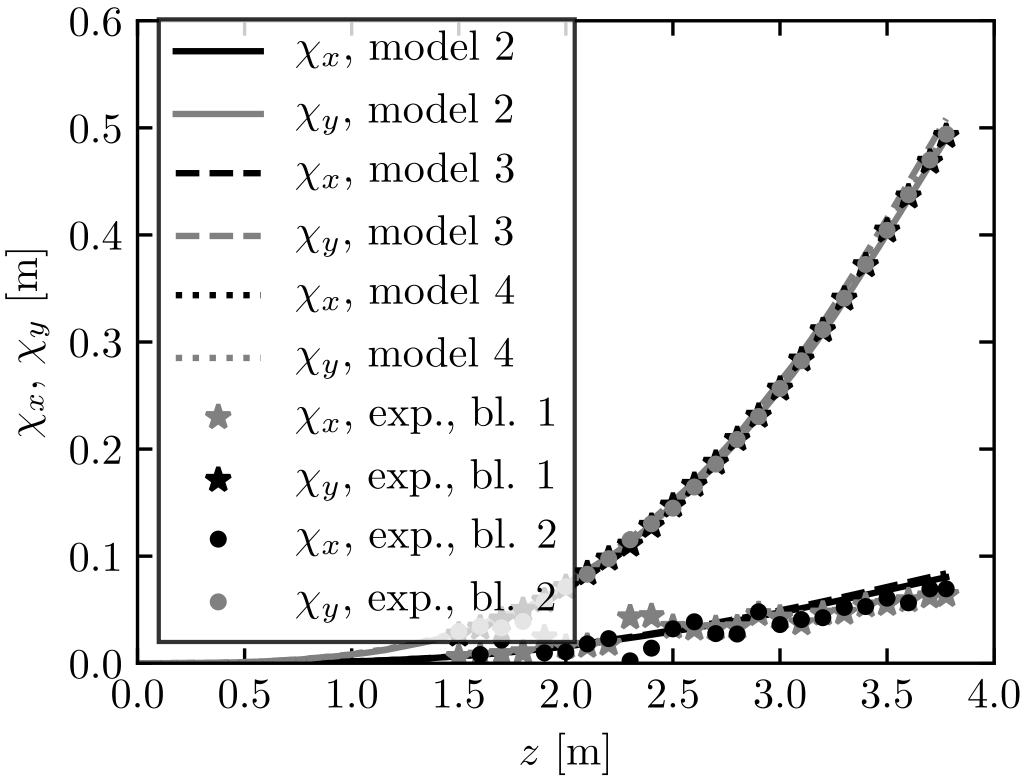
χ_x, model 2
χ_y, model 2
χ_x, model 3
χ_y, model 3
χ_x, model 4
χ_y, model 4
χ_x, exp., bl. 1
χ_y, exp., bl. 1
χ_x, exp., bl. 2
χ_y, exp., bl. 2
χ_x, χ_y [m]
z [m]
0.0
0.1
0.2
0.3
0.4
0.5
0.6
0.0
0.5
1.0
1.5
2.0
2.5
3.0
3.5
4.0

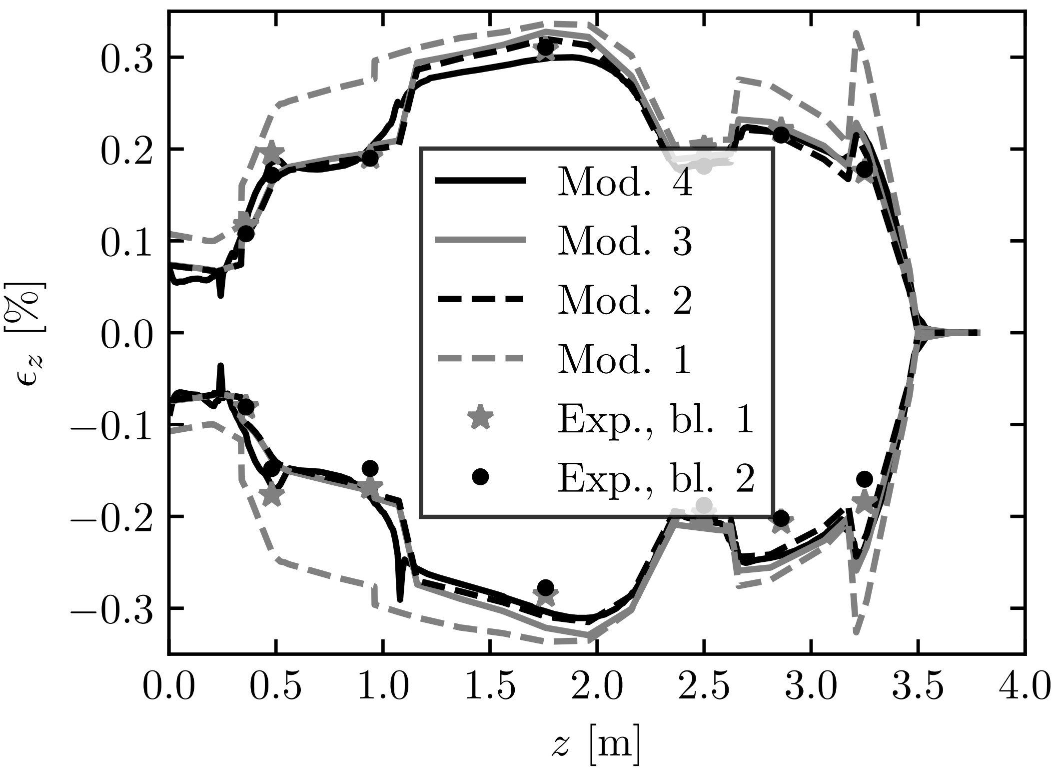
Mod. 4
Mod. 3
Mod. 2
Mod. 1
Exp., bl. 1
Exp., bl. 2
ϵ_z [%]
z [m]
0.3
0.2
0.1
0.0
−0.1
−0.2
−0.3
0.0
0.5
1.0
1.5
2.0
2.5
3.0
3.5
4.0

Journal of Renewable and Sustainable Energy

PLEASE CITE THIS ARTICLE AS DOI: 10.1063/5.0087613

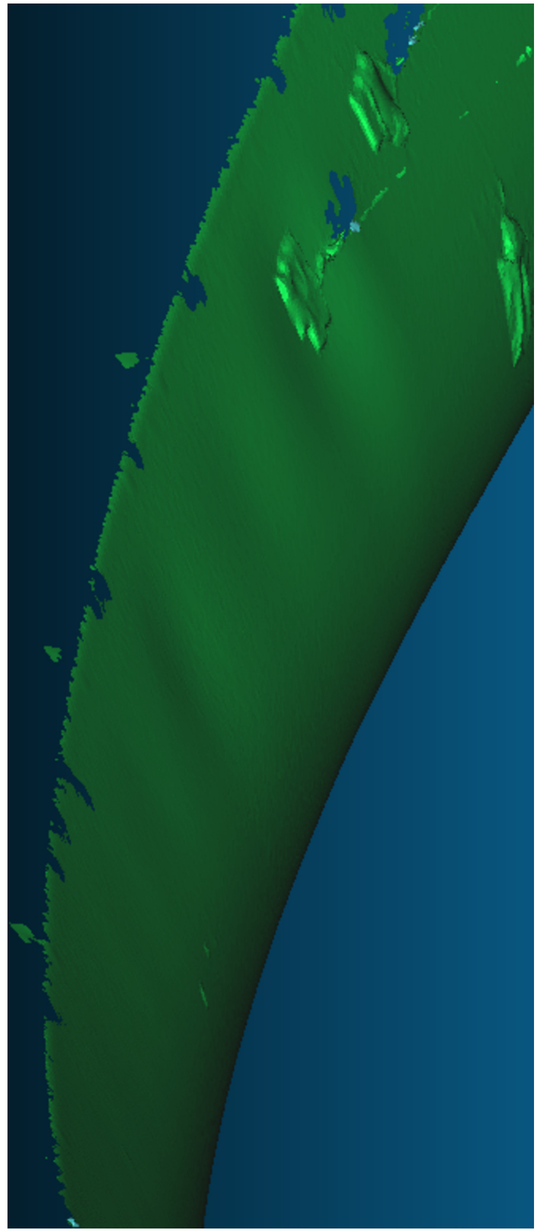

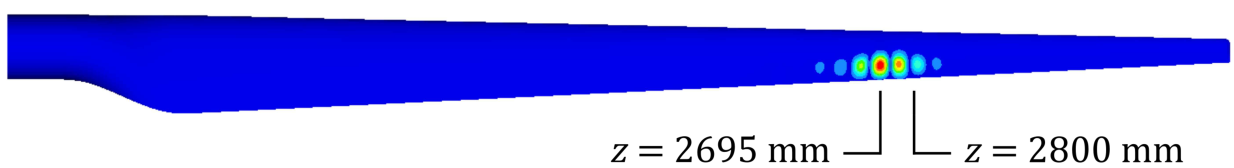
$z = 2695$ mm
$z = 2800$ mm

PLEASE CITE THIS ARTICLE AS DOI: 10.1063/5.0087613

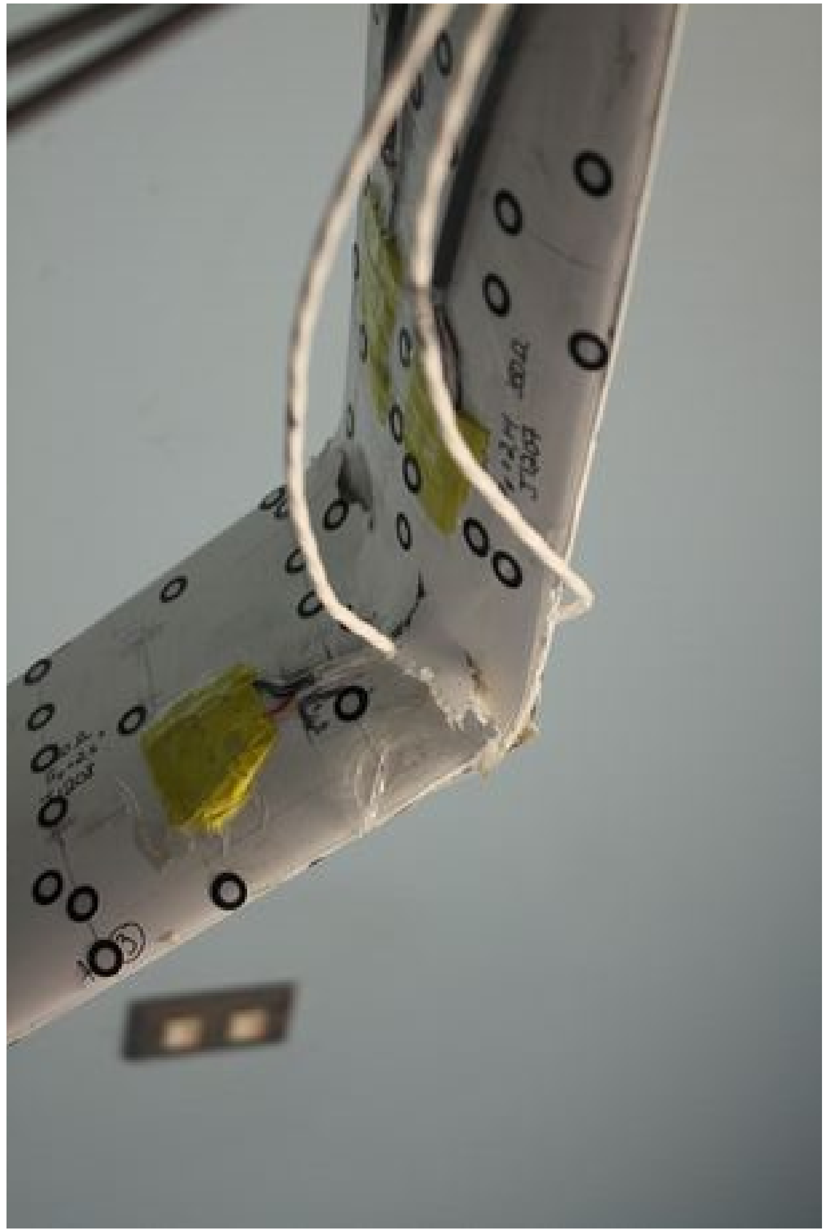

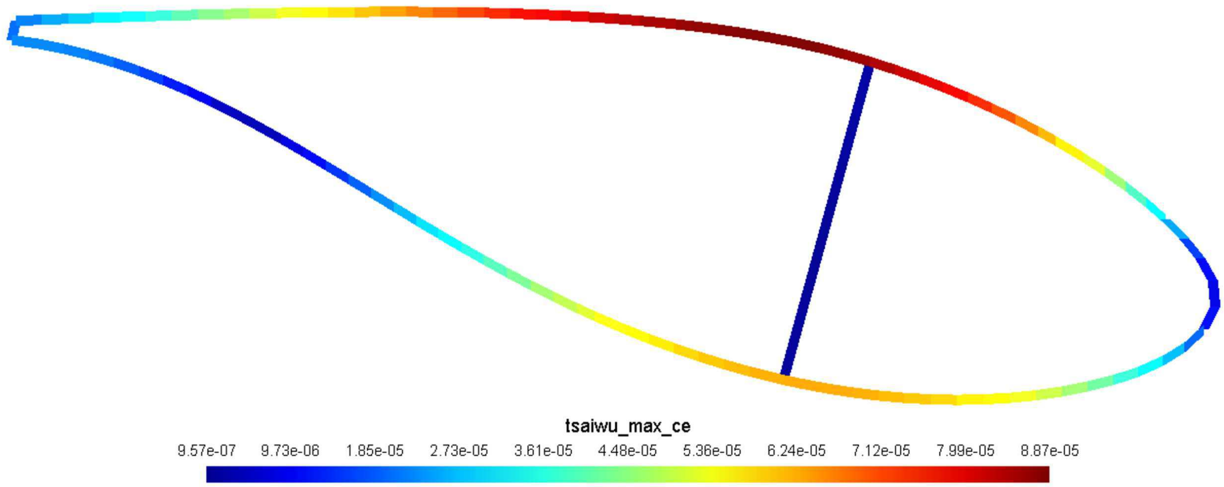
tsaiwu_max_ce
9.57e-07
9.73e-06
1.85e-05
2.73e-05
3.61e-05
4.48e-05
5.36e-05
6.24e-05
7.12e-05
7.99e-05
8.87e-05

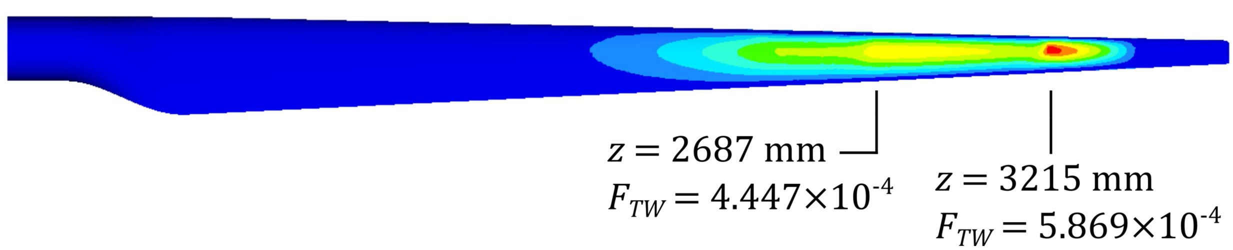
$z = 2687$ mm
$F_{TW} = 4.447\times10^{-4}$
$z = 3215$ mm
$F_{TW} = 5.869\times10^{-4}$

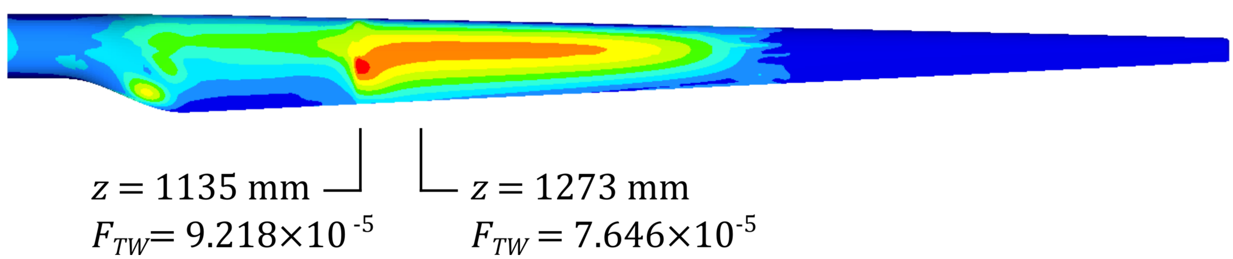
$z = 1135$ mm
$F_{TW} = 9.218\times10^{-5}$
$z = 1273$ mm
$F_{TW} = 7.646\times10^{-5}$

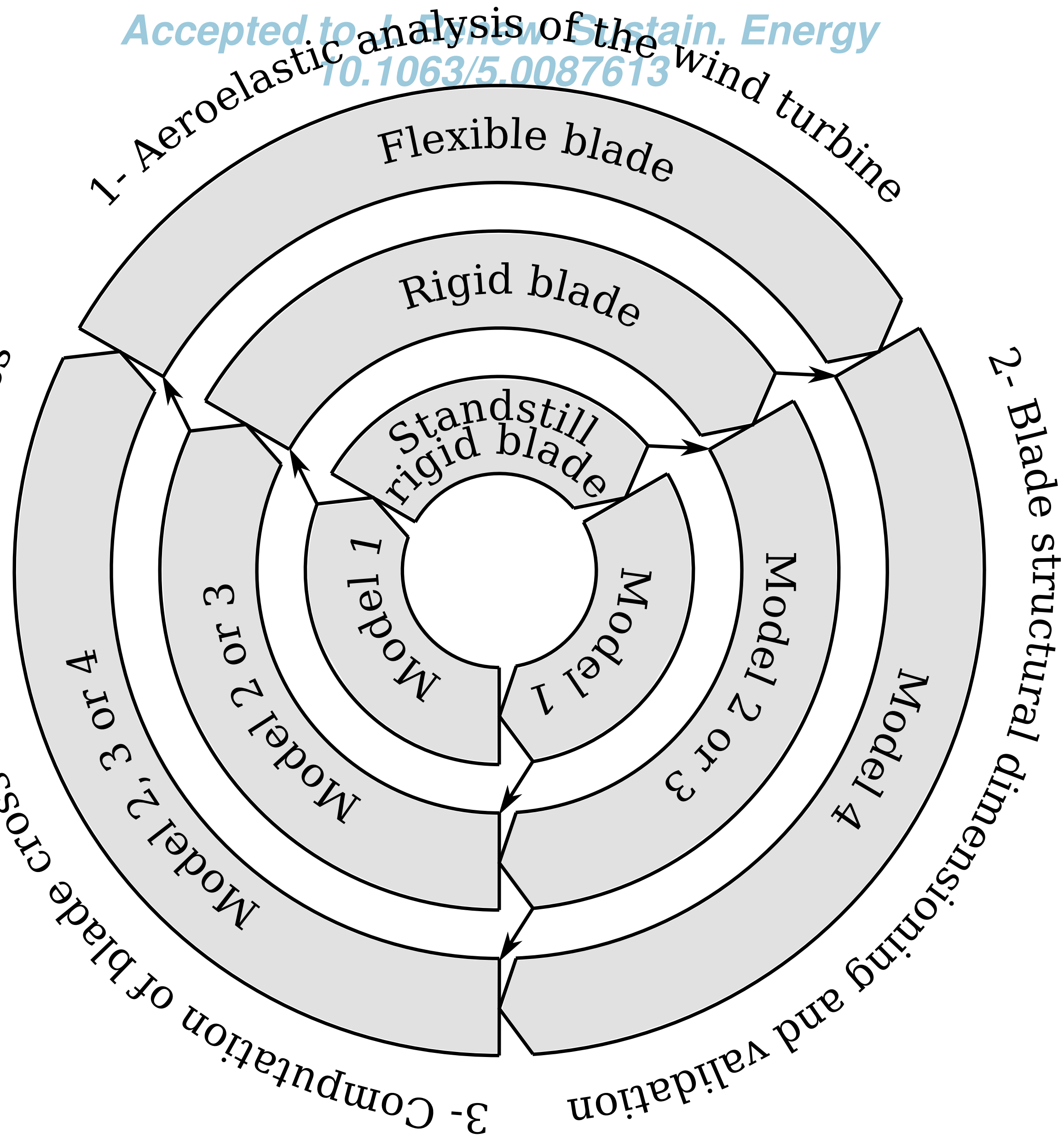
1- Aeroelastic analysis of the wind turbine
Flexible blade
Rigid blade
Standstill rigid blade
2- Blade structural dimensioning and validation
Model 1
Model 2 or 3
Model 4
3- Computation of blade cross-sectional properties
Model 1
Model 2 or 3
Model 2, 3 or 4